# The JCMT BISTRO Survey

**Citing this paper**
Please note that where the full-text provided on Manchester Research Explorer is the Author Accepted Manuscript or Proof version this may differ from the final Published version. If citing, it is advised that you check and use the publisher's definitive version.

CrossMark

# The JCMT BISTRO Survey: The Magnetic Field in the Starless Core ρ Ophiuchus C

Junhao Liu[1,2,3], Keping Qiu[1,2], David Berry[4], James Di Francesco[5,6], Pierre Bastien[7,8], Patrick M. Koch[9], Ray S. Furuya[10,11], Kee-Tae Kim[12], Simon Coudé[8,13], Chang Won Lee[12,14], Archana Soam[13,12], Chakali Eswaraiah[15], Di Li[16,17], Jihye Hwang[12,14], A-Ran Lyo[12,14], Kate Pattle[15], Tetsuo Hasegawa[19], Woojin Kwon[12,14], Shih-Ping Lai[9,15], Derek Ward-Thompson[20], Tao-Chung Ching[16,18], Zhiwei Chen[21], Qilao Gu[22], Dalei Li[23], Hua-bai Li[22], Hong-Li Liu[22], Lei Qian[16], Hongchi Wang[21], Jinghua Yuan[18], Chuan-Peng Zhang[16,18], Guoyin Zhang[16], Ya-Peng Zhang[22], Jianjun Zhou[23], Lei Zhu[16], Philippe André[24], Doris Arzoumanian[25], Yusuke Aso[26], Do-Young Byun[12,14], Michael Chun-Yuan Chen[6], Huei-Ru Vivien Chen[15], Wen Ping Chen[27], Jungyeon Cho[28], Minho Choi[12], Antonio Chrysostomou[29], Eun Jung Chung[12], Yasuo Doi[30], Emily Drabek-Maunder[31], C. Darren Dowell[32], Stewart P. S. Eyres[20], Sam Falle[33], Lapo Fanciullo[9], Jason Fiege[34], Erica Franzmann[34], Per Friberg[4], Rachel K. Friesen[35], Gary Fuller[36], Tim Gledhill[29], Sarah F. Graves[4], Jane S. Greaves[31], Matt J. Griffin[31], Ilseung Han[12,14], Jennifer Hatchell[37], Saeko S. Hayashi[38], Thiem Hoang[12,14], Wayne Holland[39,40], Martin Houde[41], Tsuyoshi Inoue[25], Shu-ichiro Inutsuka[25], Kazunari Iwasaki[42], Il-Gyo Jeong[12], Doug Johnstone[5,6], Yoshihiro Kanamori[30], Ji-hyun Kang[12], Miju Kang[12], Sung-ju Kang[12], Akimasa Kataoka[43], Koji S. Kawabata[44,45,46], Francisca Kemper[9], Gwanjeong Kim[12,14,47], Jongsoo Kim[12,14], Kyoung Hee Kim[48], Mi-Ryang Kim[12], Shinyoung Kim[12,14], Jason M. Kirk[20], Masato I. N. Kobayashi[25], Takayoshi Kusune[25], Jungmi Kwon[49], Kevin M. Lacaille[50,51], Chin-Fei Lee[9,52], Jeong-Eun Lee[53], Hyeseung Lee[28], Sang-Sung Lee[12,14], Sheng-Yuan Liu[9], Tie Liu[4,12], Sven van Loo[54], Steve Mairs[4], Masafumi Matsumura[55], Brenda C. Matthews[5,6], Gerald H. Moriarty-Schieven[5], Tetsuya Nagata[56], Fumitaka Nakamura[43,57], Hiroyuki Nakanishi[58], Nagayoshi Ohashi[38], Takashi Onaka[26], Josh Parker[20], Harriet Parsons[4], Enzo Pascale[31], Nicolas Peretto[31], Andy Pon[41], Tae-Soo Pyo[38,57], Ramprasad Rao[9], Mark G. Rawlings[4], Brendan Retter[31], John Richer[59,60], Andrew Rigby[31], Jean-François Robitaille[36], Sarah Sadavoy[3], Hiro Saito[61], Giorgio Savini[62], Anna M. M. Scaife[36], Masumichi Seta[63], Hiroko Shinnaga[64], Motohide Tamura[19,26,65], Ya-Wen Tang[9], Kohji Tomisaka[43,57], Yusuke Tsukamoto[64], Jia-Wei Wang[15], Anthony P. Whitworth[31], Hsi-Wei Yen[9,66], Hyunju Yoo[12], and Tetsuya Zenko[56]

[1] School of Astronomy and Space Science, Nanjing University, 163 Xianlin Avenue, Nanjing 210023, People's Republic of China; kpqiu@nju.edu.cn
[2] Key Laboratory of Modern Astronomy and Astrophysics (Nanjing University), Ministry of Education, Nanjing 210023, People's Republic of China
[3] Harvard-Smithsonian Center for Astrophysics, 60 Garden Street, Cambridge, MA 02138, USA
[4] East Asian Observatory, 660 N. A'ohōkū Place, University Park, Hilo, HI 96720, USA
[5] NRC Herzberg Astronomy and Astrophysics, 5071 West Saanich Road, Victoria, BC V9E 2E7, Canada
[6] Department of Physics and Astronomy, University of Victoria, Victoria, BC V8P 1A1, Canada
[7] Institut de Recherche sur les Exoplanètes (iREx), Université de Montréal, Département de Physique, C.P. 6128 Succ. Centre-ville, Montréal, QC, H3C 3J7, Canada
[8] Centre de Recherche en Astrophysique du Québec (CRAQ), Université de Montréal, Département de Physique, C.P. 6128 Succ. Centre-ville, Montréal, QC, H3C 3J7, Canada
[9] Academia Sinica Institute of Astronomy and Astrophysics, P.O. Box 23-141, Taipei 10617, Taiwan
[10] Tokushima University, Minami Jousanajima-machi 1-1, Tokushima 770-8502, Japan
[11] Institute of Liberal Arts and Sciences Tokushima University, Minami Jousanajima-machi 1-1, Tokushima 770-8502, Japan
[12] Korea Astronomy and Space Science Institute (KASI), 776 Daedeokdae-ro, Yuseong-gu, Daejeon 34055, Republic of Korea
[13] SOFIA Science Center, Universities Space Research Association, NASA Ames Research Center, M.S. N232-12, Moffett Field, CA 94035, USA
[14] University of Science and Technology, Korea (UST), 217 Gajeong-ro, Yuseong-gu, Daejeon 34113, Republic of Korea
[15] Institute of Astronomy and Department of Physics, National Tsing Hua University, Hsinchu 30013, Taiwan
[16] CAS Key Laboratory of FAST, National Astronomical Observatories of China (NAOC), Chinese Academy of Sciences, People's Republic of China
[17] University of Chinese Academy of Sciences, Beijing 100049, People's Republic of China
[18] National Astronomical Observatories, Chinese Academy of Sciences, A20 Datun Road, Chaoyang District, Beijing 100012, People's Republic of China
[19] National Astronomical Observatory of Japan, National Institutes of Natural Sciences, Osaka, Mitaka, Tokyo 181-8588, Japan
[20] Jeremiah Horrocks Institute, University of Central Lancashire, Preston PR1 2HE, UK
[21] Purple Mountain Observatory, Chinese Academy of Sciences, 2 West Beijing Road, 210008 Nanjing, People's Republic of China
[22] Department of Physics, The Chinese University of Hong Kong, Shatin, N.T., Hong Kong
[23] Xinjiang Astronomical Observatory, Chinese Academy of Sciences, 150 Science 1-Street, Urumqi 830011, Xinjiang, People's Republic of China
[24] Laboratoire AIM CEA/DSM-CNRS-Universit Paris Diderot, IRFU/Service dAstrophysique, CEA Saclay, F-91191 Gif-sur-Yvette, France
[25] Department of Physics, Graduate School of Science, Nagoya University, Furo-cho, Chikusa-ku, Nagoya 464-8602, Japan
[26] Department of Astronomy, Graduate School of Science, The University of Tokyo, 7-3-1 Hongo, Bunkyo-ku, Tokyo 113-0033, Japan
[27] Institute of Astronomy, National Central University, Chung-Li 32054, Taiwan
[28] Department of Astronomy and Space Science, Chungnam National University, 99 Daehak-ro, Yuseong-gu, Daejeon 34134, Republic of Korea
[29] School of Physics, Astronomy & Mathematics, University of Hertfordshire, College Lane, Hatfield, Hertfordshire AL10 9AB, UK
[30] Department of Earth Science and Astronomy, Graduate School of Arts and Sciences, The University of Tokyo, 3-8-1 Komaba, Meguro, Tokyo 153-8902, Japan
[31] School of Physics and Astronomy, Cardiff University, The Parade, Cardiff, CF24 3AA, UK
[32] Jet Propulsion Laboratory, M/S 169-506, 4800 Oak Grove Drive, Pasadena, CA 91109, USA
[33] Department of Applied Mathematics, University of Leeds, Woodhouse Lane, Leeds LS2 9JT, UK
[34] Department of Physics and Astronomy, The University of Manitoba, Winnipeg, Manitoba R3T2N2, Canada
[35] National Radio Astronomy Observatory, 520 Edgemont Road, Charlottesville, VA 22903, USA
[36] Jodrell Bank Centre for Astrophysics, School of Physics and Astronomy, University of Manchester, Oxford Road, Manchester, M13 9PL, UK
[37] Physics and Astronomy, University of Exeter, Stocker Road, Exeter EX4 4QL, UK
[38] Subaru Telescope, National Astronomical Observatory of Japan, 650 N. A'ohōkū Place, University Park, Hilo, HI 96720, USA
[39] UK Astronomy Technology Centre, Royal Observatory, Blackford Hill, Edinburgh EH9 3HJ, UK
[40] Institute for Astronomy, University of Edinburgh, Royal Observatory, Blackford Hill, Edinburgh EH9 3HJ, UK

[41] Department of Physics and Astronomy, The University of Western Ontario, 1151 Richmond Street, London N6A 3K7, Canada
[42] Department of Environmental Systems Science, Doshisha University, Tatara, Miyakodani 1-3, Kyotanabe, Kyoto 610-0394, Japan
[43] Division of Theoretical Astronomy, National Astronomical Observatory of Japan, Mitaka, Tokyo 181-8588, Japan
[44] Hiroshima Astrophysical Science Center, Hiroshima University, Kagamiyama 1-3-1, Higashi-Hiroshima, Hiroshima 739-8526, Japan
[45] Department of Physics, Hiroshima University, Kagamiyama 1-3-1, Higashi-Hiroshima, Hiroshima 739-8526, Japan
[46] Core Research for Energetic Universe (CORE-U), Hiroshima University, Kagamiyama 1-3-1, Higashi-Hiroshima, Hiroshima 739-8526, Japan
[47] Nobeyama Radio Observatory (NRO), National Astronomical Observatory of Japan (NAOJ), Japan
[48] Department of Earth Science Education, Kongju National University, 56 Gongjudaehak-ro, Gongju-si, Chungcheongnam-do 32588, Republic of Korea
[49] Institute of Space and Astronautical Science, Japan Aerospace Exploration Agency, 3-1-1 Yoshinodai, Chuo-ku, Sagamihara, Kanagawa 252-5210, Japan
[50] Department of Physics and Astronomy, McMaster University, Hamilton, ON L8S 4M1, Canada
[51] Department of Physics and Atmospheric Science, Dalhousie University, Halifax B3H 4R2, Canada
[52] Graduate Institute of Astronomy and Astrophysics, National Taiwan University, No. 1, Sec. 4, Roosevelt Road, Taipei 10617, Taiwan
[53] School of Space Research, Kyung Hee University, 1732 Deogyeong-daero, Giheung-gu, Yongin-si, Gyeonggi-do 17104, Republic of Korea
[54] School of Physics and Astronomy, University of Leeds, Woodhouse Lane, Leeds LS2 9JT, UK
[55] Kagawa University, Saiwai-cho 1-1, Takamatsu, Kagawa, 760-8522, Japan
[56] Department of Astronomy, Graduate School of Science, Kyoto University, Sakyo-ku, Kyoto 606-8502, Japan
[57] SOKENDAI (The Graduate University for Advanced Studies), Hayama, Kanagawa 240-0193, Japan
[58] Department of Physics and Astronomy, Graduate School of Science and Engineering, Kagoshima University, 1-21-35 Korimoto, Kagoshima, Kagoshima 890-0065, Japan
[59] Astrophysics Group, Cavendish Laboratory, J. J. Thomson Avenue, Cambridge CB3 0HE, UK
[60] Kavli Institute for Cosmology, Institute of Astronomy, University of Cambridge, Madingley Road, Cambridge, CB3 0HA, UK
[61] Department of Astronomy and Earth Sciences, Tokyo Gakugei University, Koganei, Tokyo 184-8501, Japan
[62] OSL, Physics & Astronomy Dept., University College London, WC1E 6BT London, UK
[63] Department of Physics, School of Science and Technology, Kwansei Gakuin University, 2-1 Gakuen, Sanda, Hyogo 669-1337, Japan
[64] Department of Physics and Astronomy, Graduate School of Science and Engineering, Kagoshima University, 1-21-35 Korimoto, Kagoshima, Kagoshima 890-0065, Japan
[65] Astrobiology Center, National Institutes of Natural Sciences, 2-21-1 Osawa, Mitaka, Tokyo 181-8588, Japan
[66] European Southern Observatory (ESO), Karl-Schwarzschild-Strasse 2, D-85748 Garching, Germany

## Abstract

We report 850 $\mu$m dust polarization observations of a low-mass ($\sim$12 $M_\odot$) starless core in the $\rho$ Ophiuchus cloud, Ophiuchus C, made with the POL-2 instrument on the James Clerk Maxwell Telescope (JCMT) as part of the JCMT *B*-fields In STar-forming Region Observations survey. We detect an ordered magnetic field projected on the plane of the sky in the starless core. The magnetic field across the $\sim$0.1 pc core shows a predominant northeast–southwest orientation centering between $\sim$40° and $\sim$100°, indicating that the field in the core is well aligned with the magnetic field in lower-density regions of the cloud probed by near-infrared observations and also the cloud-scale magnetic field traced by *Planck* observations. The polarization percentage ($P$) decreases with increasing total intensity ($I$), with a power-law index of $-1.03 \pm 0.05$. We estimate the plane-of-sky field strength ($B_{\rm pos}$) using modified Davis–Chandrasekhar–Fermi methods based on structure function (SF), autocorrelation function (ACF), and unsharp masking (UM) analyses. We find that the estimates from the SF, ACF, and UM methods yield strengths of $103 \pm 46\,\mu$G, $136 \pm 69\,\mu$G, and $213 \pm 115\,\mu$G, respectively. Our calculations suggest that the Ophiuchus C core is near magnetically critical or slightly magnetically supercritical (i.e., unstable to collapse). The total magnetic energy calculated from the SF method is comparable to the turbulent energy in Ophiuchus C, while the ACF method and the UM method only set upper limits for the total magnetic energy because of large uncertainties.

*Key words:* ISM: individual objects (Ophiuchus) – magnetic fields – polarization – stars: formation

## 1. Introduction

The role of magnetic fields (*B*-fields) has long been a hot topic under debate in star formation studies (Crutcher 2012). There are two major classes of star formation theories that significantly differ in the role played by magnetic fields. "Strong magnetic field models" suggest that molecular clouds are supported by magnetic fields, which quasi-statically dissipate via ambipolar diffusion. Eventually self-gravity overcomes the magnetic force, inducing the collapse of molecular cloud cores and the formation of stars (Mouschovias et al. 2006). In contrast, "weak-field models" suggest that turbulent flows, instead of magnetic fields, dominate the evolution of molecular clouds and create overdense regions where stars form (Mac Low & Klessen 2004). Recently, results from simulations indicate that magnetic field and turbulence are both essential to provide support against gravitational collapse (Padoan et al. 2014, and references therein). Observational

studies of magnetic fields in star-forming regions can directly test these theoretical models, providing deep insights into the relative importance of magnetic fields and gravity/turbulence in cloud evolution and star formation.

Observing the polarized emission of dust grains and the polarization of background stars is one of the powerful ways to investigate the plane-of-sky magnetic field structure in star-forming regions (Hildebrand 1988b). The starlight polarization was first discovered by Hiltner (1949) and Hall (1949). Later on, the observed polarization of starlight was explained by the partial extinction of starlight by magnetically aligned dust grains (Hildebrand 1988a), where the short axes of spinning dust grains align with magnetic field lines. This explanation is widely accepted. There are many theories trying to explain why dust grains are aligned with magnetic fields. Among them, the Radiative Alignment Torque (RAT) theory is most accepted (Lazarian 2007 Lazarian & Hoang 2007). Although the details of the gain alignment mechanism are still unclear, the plane-of-sky

magnetic field structure in star formation regions has been successfully traced using polarization observations (Crutcher 2012). Polarization observations at near-infrared (NIR) wavelengths, which are expected to trace polarization produced by dust extinction of background starlight, are often used to investigate the magnetic field structure in dense molecular regions (Santos et al. 2014; Kwon et al. 2015). However, NIR polarization observations are not sufficient to trace the magnetic field in regions with high extinction or associated with few background stars. Polarization observations at submillimeter wavelengths, which trace dust thermal emission, are essential to overcome the drawback of NIR polarization observations and to probe the magnetic field structure in denser environments such as filaments and dense cores.

Among an increasing number of polarization observations toward low-mass star formation regions, studies of the protostellar phase of young stellar objects have attracted the most interest. One important approach of these studies is to find hourglass-shaped magnetic fields. As predicted by the theoretical model and simulations (Galli & Shu 1993a, 1993b), the magnetic field of magnetically dominated dense regions is expected to show an hourglass shape in the collapse phase. At 0.001–0.01 pc scales, dust polarization observations toward low-mass protostellar systems have revealed the expected hourglass-shaped field morphologies (Girart et al. 2006; Rao et al. 2009; Stephens et al. 2013). More chaotic field morphologies, which are expected in weakly magnetic environments or probably affected by stellar feedback or complex geometry, are also reported at this scale (Hull et al. 2014, 2017). At larger scales (0.01–0.1 pc), hints of the hourglass shape are less obvious (Matthews et al. 2009; Dotson et al. 2010; Hull et al. 2014), and the role of magnetic field at this scale is comparatively less understood.

Since the magnetic field in protostellar cores can suffer from feedback by star-forming activities, polarization studies of starless cores are essential to help us understand the role of magnetic fields in the early stages of star formation. The relatively weak polarized dust emission in starless cores, however, is far more difficult to detect, and as a result, there are only a handful of dust polarization observations toward starless cores (Ward-Thompson et al. 2000, 2009; Crutcher et al. 2004; Alves et al. 2014). The role of magnetic fields in the initial phase of star formation remains an open question.

The Ophiuchus molecular cloud is a low-mass star-forming region located at a distance of ∼137 pc (Ortiz-León et al. 2017). It is one of the nearest star formation regions and has been widely studied (Wilking et al. 2008, and references therein). Star formation in this cloud is heavily influenced by compression of expanding shock shells from the nearby Sco-Cen OB association (Vrba 1977). A detailed DCO$^+$ emission study has identified several dense cores, Ophiuchus A to Ophiuchus F (hereafter Oph-A to Oph-F), in the main body of Ophiuchus (Loren et al. 1990). Among these dense cores, our target, Oph-C, which harbors no embedded protostars (Enoch et al. 2009) and is not associated with *Herschel* 70 μm emission (Pattle et al. 2015), appears to be the least evolved and is extremely quiescent. The 850 μm continuum of Oph-C was observed as part of the James Clerk Maxwell telescope (JCMT) Gould Belt Survey (GBS; Ward-Thompson et al. 2007; Pattle et al. 2015). Pattle et al. (2015) identified a few low-mass, pressure-confined, virially bound, and ∼0.01 pc scale (∼3000 au) subcores in Oph-C based on the GBS data. The 850 μm polarization data of the Ophiuchus cloud obtained using SCUPOL, the previous JCMT polarimeter, were cataloged by Matthews et al. (2009). More recently, the

large-scale plane-of-sky magnetic field map of the Ophiuchus cloud was presented by Planck Collaboration et al. (2015) at 5′ resolution as part of the *Planck* project. Kwon et al. (2015) conducted NIR polarimetry of the Ophiuchus cloud and suggested that the magnetic field structures in the cloud may have been influenced by the nearby Sco-Cen OB association.

Here we present 850 μm dust polarization observations using the POL-2 polarimeter in combination with the Submillimetre Common-User Bolometer Array 2 (SCUBA-2) on the JCMT toward the Oph-C region as part of the *B*-fields In STar-forming Region Observations (BISTRO) survey (Ward-Thompson et al. 2017). The BISTRO survey is aimed at using POL-2 to map the polarized dust emission in the densest parts of all of the Gould Belt star-forming regions, including Orion A (Pattle et al. 2017), Oph-A (Kwon et al. 2018), M16 (Pattle et al. 2018), Oph-B (Soam et al. 2018), and several other regions (papers in preparation). With the unique resolution offered by JCMT, which can resolve the magnetic field structures down to scales of ∼1000 au in nearby star formation regions, these POL-2 observations are crucial to test theoretical models of star formation at an intermediate scale and to generate a large sample of polarization maps of dense cores obtained in a uniform and consistent way for statistical studies (Ward-Thompson et al. 2017). The *B*-field structures traced by POL-2 agree well with those traced by the previous SCUPOL observations, but the POL-2 maps are more sensitive than the previous SCUPOL data and trace larger areas (e.g., Kwon et al. 2018; Soam et al. 2018).

This paper is organized as follows: in Section 2, we describe the observations and data reduction; in Section 3, we present the results of the observations and derive the *B*-field strength; in Section 4, we discuss our results; and in Section 5, we provide a summary of this paper.

## 2. Observations

The polarized emission of Oph-C was observed at 850 μm with SCUBA-2 (Holland et al. 2013) along with POL-2 (Friberg et al. 2016; P. B. Bastien et al. 2019, in preparation) between 2016 May 22 and September 10. The region was observed 20 times, among which 19 data sets had an average integration time of 42 minutes and one bad data set was excluded. The observations were made with the POL-2 DAISY mode, which produces a map with high signal-to-noise ratio (S/N) at a central region of 3′ radius and with increasing noise to the edge. The effective beam size of JCMT is 14″1 (∼9 mpc 137 pc) at 850 μm.

The data were reduced using the SMURF (Jenness et al. 2013) package in Starlink (Currie et al. 2014). First, the *calcqu* command is used to convert the raw bolometer time streams into separate Stokes *I*, *Q*, and *U* time streams. Then, the *makemap* routine in the *pol2map* script creates individual *I* maps from the *I* time streams of each observation and co-adds them to produce an initial reference *I* map. Second, the *pol2map* is rerun with the initial *I* map to generate an ASTMASK, which is used to define the S/N-based background regions that are set to zero until the last iteration, and a PCAMASK, which defines the source regions that are excluded when creating the background models within *makemap*. With the ASTMASK and the PCAMASK, *pol2map* is again rerun to reduce the previously created *I* time streams of each observation, creating improved *I* maps. These individual improved *I* maps are then co-added to produce a final improved *I* map. Finally, with the same masks, *pol2map* creates the

(a)



(b)



(c)
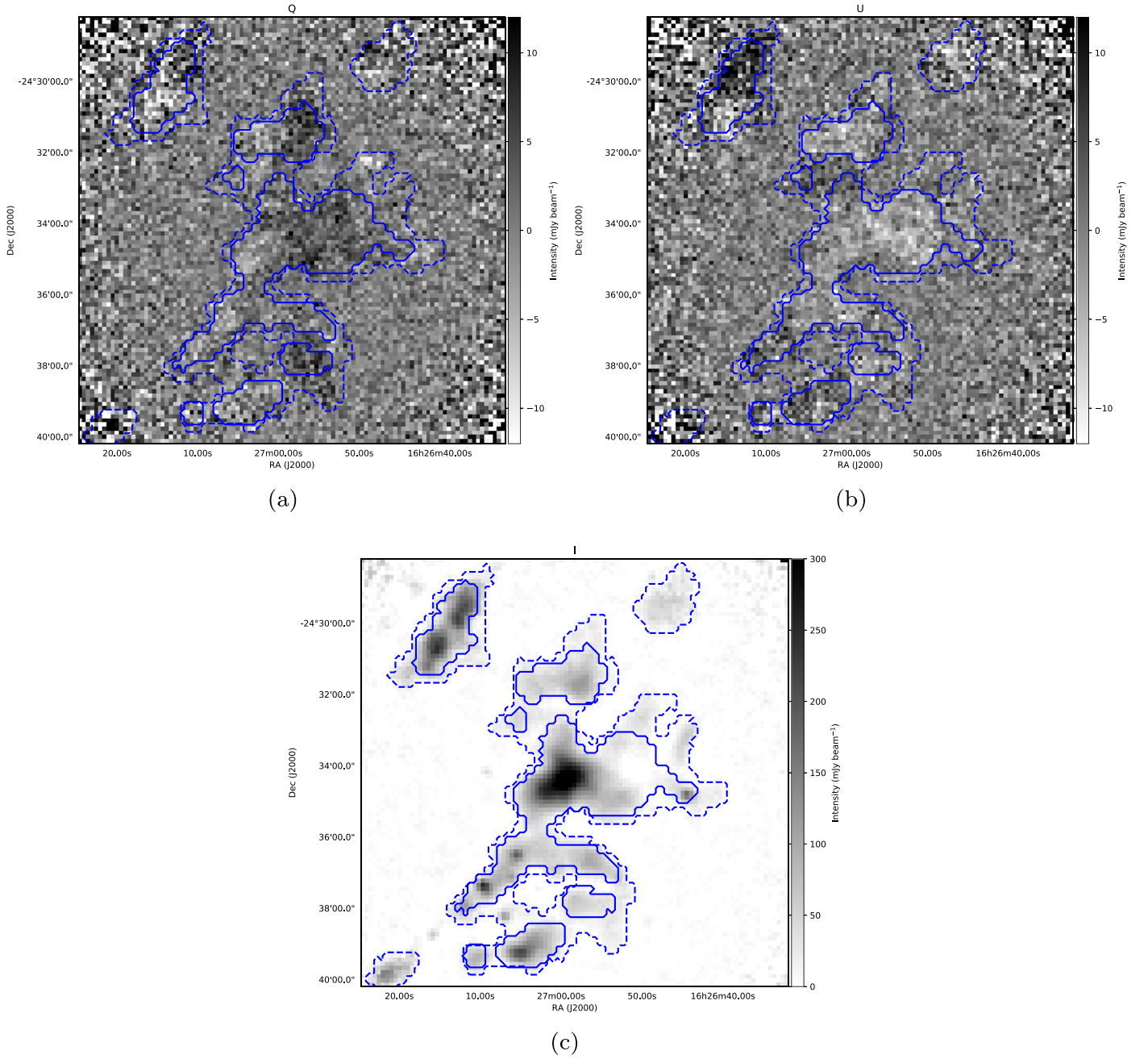
**Figure 1.** (a–c) POL-2 Stokes $Q$, $U$, and $I$ maps of the Oph-C region, respectively. The intensity is shown in gray scale. The ASTMASK and the PCAMASK used in the data reduction process are shown with dashed and solid lines, respectively.

$Q$ and $U$ maps, along with their variance maps, and the debiased polarization catalog, from the $Q$ and $U$ time streams. The final improved $I$ map is used for instrumental polarization correction. The final $I$, $Q$, and $U$ maps and the polarization catalog are gridded to $7''$ pixels for a Nyquist sampling.

The absolute calibration is performed by applying a flux conversion factor (FCF) of 725 Jy beam$^{-1}$ pW$^{-1}$ to the output $I$, $Q$, and $U$ maps, converting the units of these maps from pW to Jy beam$^{-1}$. Due to the additional losses from POL-2, this FCF is 1.35 times larger than the standard SCUBA-2 FCF of 537 Jy beam$^{-1}$ pW$^{-1}$ (Dempsey et al. 2013). The uncertainty on the flux calibration is 5% (Dempsey et al. 2013). Figure 1 shows the $Q$, $U$, and $I$ maps of our POL-2 data. The rms noises

of the background regions in the $Q$ or $U$ maps are $\sim$3.5 mJy beam$^{-1}$. From the corresponding variance maps, the average $Q$ or $U$ variances are $\sim$2 mJy beam$^{-1}$, reaching the target sensitivity value for the BISTRO survey.

Figure 2 shows the total intensity map toward the same region made with SCUBA-2 as part of the GBS project (Pattle et al. 2015) and the difference between the SCUBA-2 $I$ map and the POL-2 $I$ map. Because of the difference in the data reduction procedures of the POL-2 data and the SCUBA-2 data and the slower scanning speed of the POL-2 observation, the large-scale structures seen in the SCUBA-2 $I$ map are suppressed in the POL-2 $I$ map. Hence, the BISTRO $I$ map is much fainter than the GBS $I$ map.
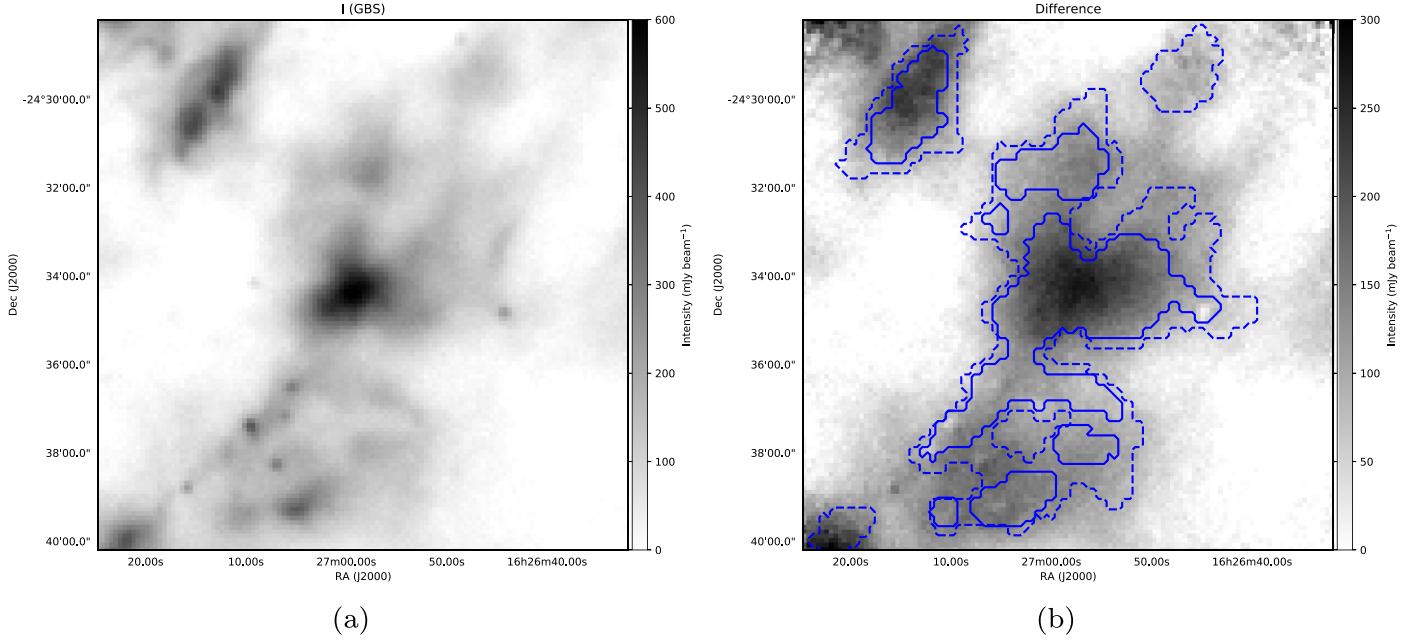
**Figure 2.** (a) SCUBA-2 850 $\mu$m *I* map obtained from the GBS project. (b) Difference map obtained by subtracting the POL-2 *I* map from the SCUBA-2 *I* map. The intensity is shown in gray scale. The masks are the same as those in Figure 1.

Because of the uncertainties in the *Q* and *U* values and given that the polarized intensity and polarized percentage are defined as positive values, the measured polarized intensities are biased toward larger values (Vaillancourt 2006). The debiased polarized intensity and its corresponding uncertainty are calculated as

$$\mathrm{PI} = \sqrt{Q^2 + U^2 - 0.5(\delta Q^2 + \delta U^2)} \qquad (1)$$

and

$$\delta \mathrm{PI} = \sqrt{\frac{(Q^2 \delta Q^2 + U^2 \delta U^2)}{(Q^2 + U^2)}}, \qquad (2)$$

where PI is the polarized intensity, $\delta Q$ is the uncertainty of *Q*, and $\delta U$ is the uncertainty of *U*. The debiased polarization percentage *P* and its uncertainty $\delta P$ are therefore derived by

$$P = \frac{\mathrm{PI}}{I} \qquad (3)$$

and

$$\delta P = \sqrt{\left(\frac{\delta \mathrm{PI}^2}{I^2} + \frac{\delta I^2 (Q^2 + U^2)}{I^4}\right)}, \qquad (4)$$

where $\delta I$ is the uncertainty of the total intensity.

Finally, the polarization position angle $\theta$ and its uncertainty $\delta\theta$ (Naghizadeh-Khouei & Clarke 1993) are estimated to be

$$\theta = \frac{1}{2} \tan^{-1}\left(\frac{U}{Q}\right) \qquad (5)$$

and

$$\delta\theta = \frac{1}{2} \sqrt{\frac{(Q^2 \delta U^2 + U^2 \delta Q^2)}{(Q^2 + U^2)^2}}, \qquad (6)$$

## 3. Results

### 3.1. The Magnetic Field Morphology in the Oph-C Region

Assuming that the shortest axis of dust grains is perfectly aligned with the magnetic field, we can derive the orientation of the magnetic field projected on the plane of the sky by rotating the observed polarization vectors by 90°. Figure 3 shows the *B*-field segments of our POL-2 observations. These segments have lengths proportional to the polarization degrees and orientations along the local *B*-field. Note that our POL-2 segments are Nyquist sampled with a pixel size of 7″. With these criteria, the vectors in the Oph-C region are well separated from those in other dense regions of the Ophiuchus cloud. The magnetic field orientations do not appear random and have a predominant northeast–southwest orientation.

Figure 4 compares the magnetic field orientations from our POL-2 data with previous observations with the older JCMT polarimeter (SCUPOL; Matthews et al. 2009). We use criteria of $P/\delta P > 2$ and $\delta P < 4\%$ for both the POL-2 data and the SCUPOL data. Compared to the previous SCUPOL observations, our POL-2 observations show significant improvements by detecting dust polarization over a much larger area and toward the center of the core.

In Figure 5, histograms of the position angles of the *B*-field segments from the POL-2 data and the SCUPOL data are shown. The POL-2 histogram has a broad peak between $\sim 40°$ and $\sim 100°$. The standard deviation of the position angles of these POL-2 vectors is $\sim 33°$. The SCUPOL vectors are randomly distributed, which is inconsistent with the POL-2 vectors.

To further compare the SCUPOL data and the POL-2 data, we resampled the POL-2 data to the same pixel size as that of the SCUPOL data (10″) and aligned the world coordinate system of the two data sets. We found 31 pairs of spatially overlapping vectors between the two data sets with vector selection criteria of $P/\delta P > 2$ and $\delta P < 4\%$. Figure 6 shows the comparison of position angles (after 90° rotation) for these
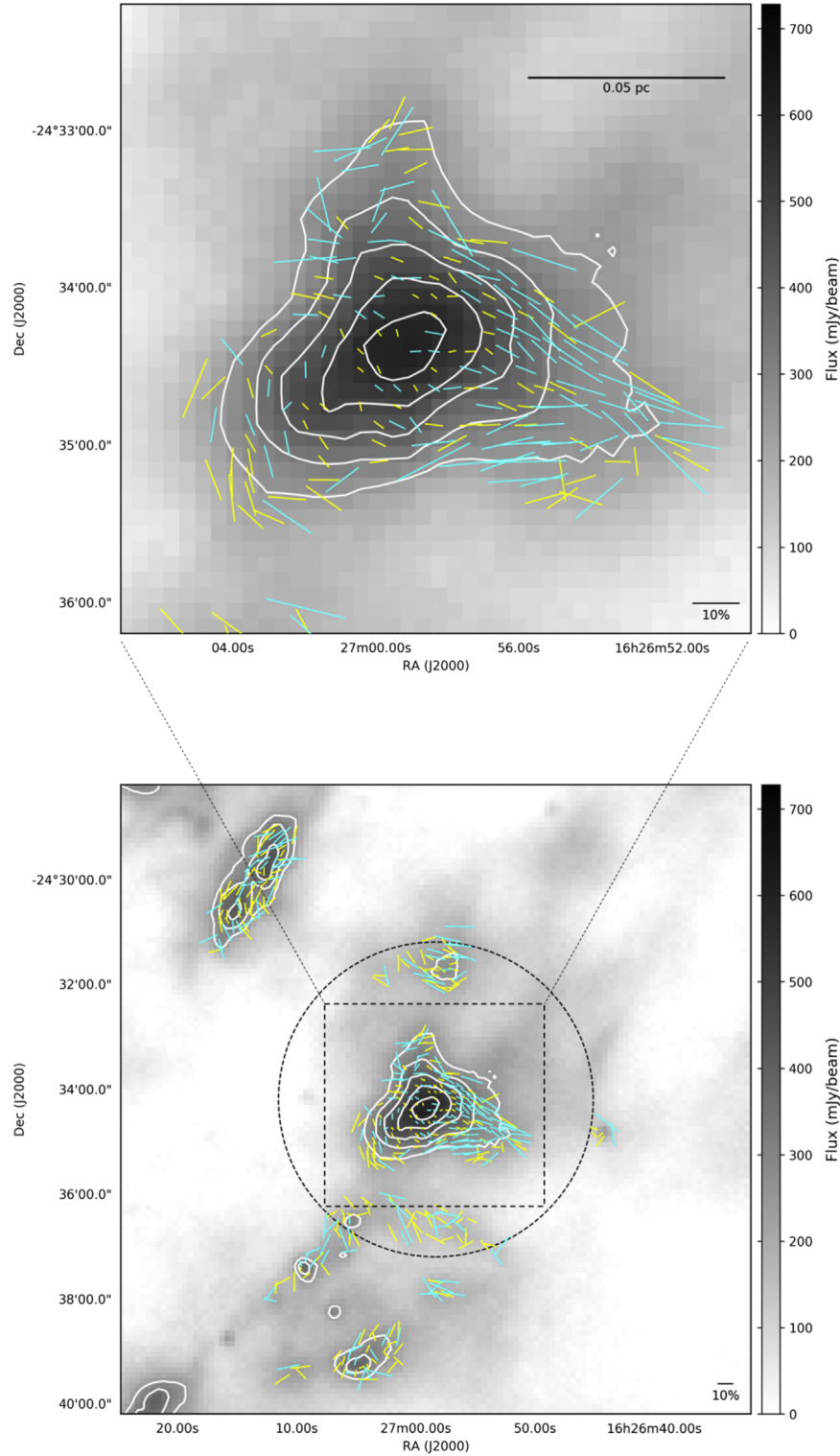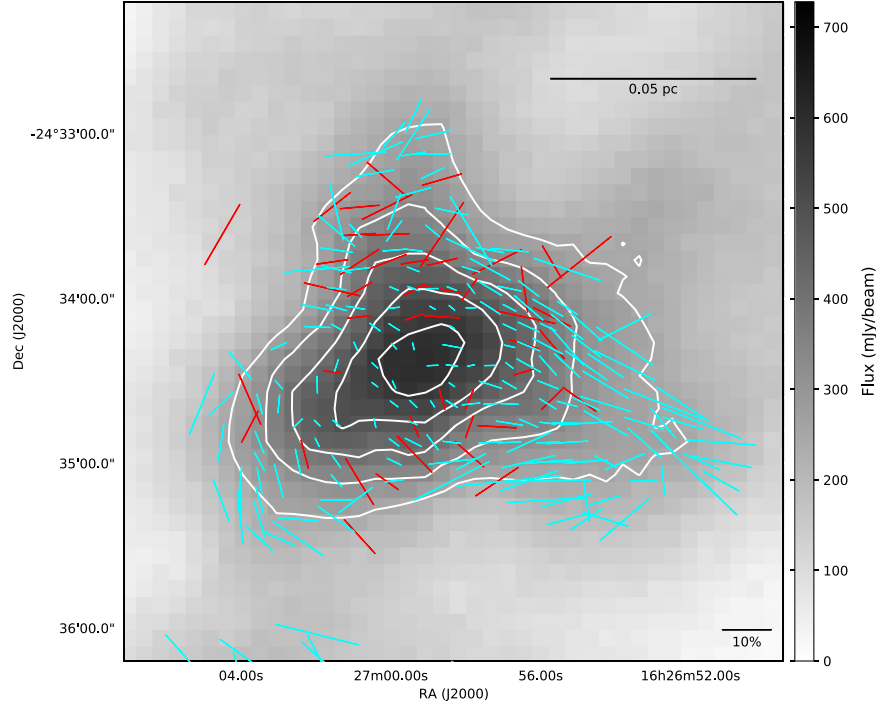
**Figure 3.** Magnetic field orientation maps. The total intensity of the 850 $\mu$m continuum from the GBS project is shown in gray scale. The total intensity is also shown in contour levels, starting from 250 mJy beam$^{-1}$ and continuing at steps of 80 mJy beam$^{-1}$. Vectors are from the POL-2 data with $\delta P < 5\%$. The yellow and cyan vectors correspond to data with $P/\delta P > 2$ and $P/\delta P > 3$, respectively. A reference 10% vector is shown in the lower right corner. A black dashed circle shows the central region of $3'$ radius.

overlapping vectors. Large angular differences in the position angles of overlapping vectors can be seen in this figure. The average angular difference of overlapping vectors is estimated to be $\sim39°$. We further computed the Kolmogorov–Smirnov (KS) statistic on the POL-2 and SCUPOL position angles and

found a probability of 0.06, which suggests the inconsistency in position angles between the two samples. Such a difference, along with the aforementioned inconsistency in histograms of the position angles, can be explained by the lower S/N of the SCUPOL data.

**Figure 4.** Magnetic field orientation maps. The gray scales and contours are the same as those in Figure 3. The cyan and red vectors denote POL-2 data and SCUPOL data, where $P/\delta P > 2$ and $\delta P < 4\%$, respectively. A reference 10% vector is shown in the lower right.
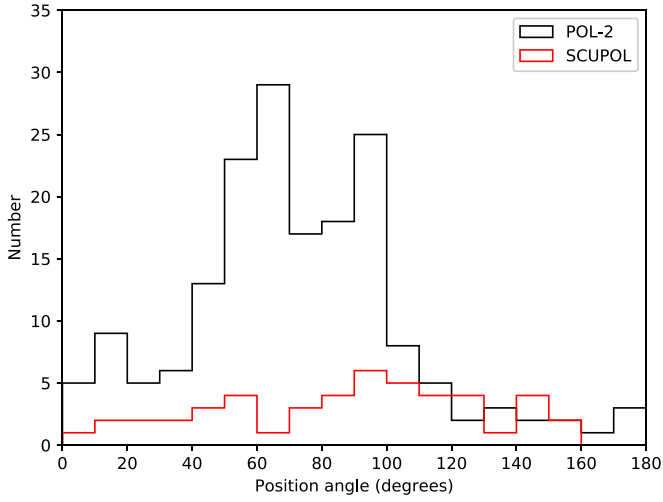


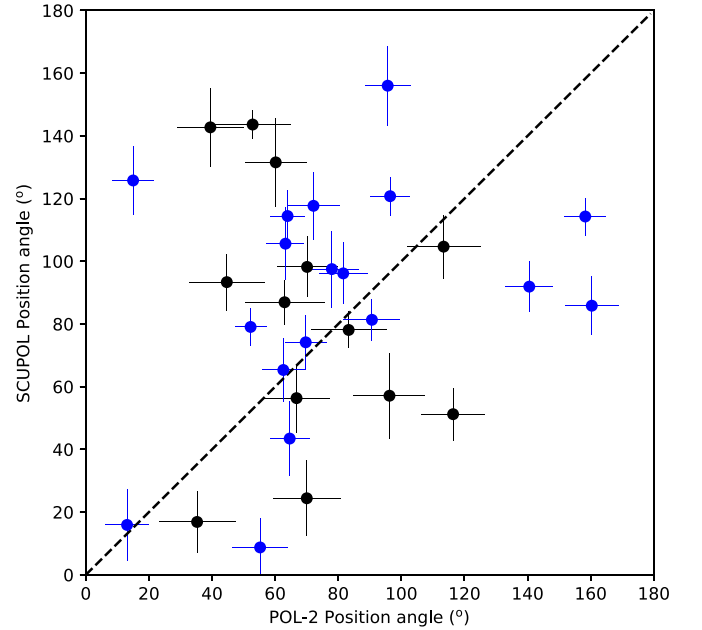**Figure 5.** Position angle (after 90° rotation) histogram for $B$-field vectors with $P/\delta P > 2$ and $\delta P < 4\%$. The bin size is 10°. The POL-2 vectors are shown in black. The SCUPOL vectors are shown in red. Angles are measured east of north.



**Figure 6.** Comparison of position angles (after 90° rotation) for overlapping SCUPOL and POL-2 vectors with $P/\delta P > 2$ and $\delta P < 4\%$. Data points correspond to POL-2 data, with values of $P/\delta P > 3$ marked in blue. Angles are measured east of north.

### 3.2. The Strength of the Magnetic Field

Davis (1951) and Chandrasekhar & Fermi (1953) proposed that the strength of the $B$-field could be estimated by interpreting the observed deviation of polarization angles from the mean polarization angle orientation as Alfvén waves induced by turbulent perturbations. This interpretation implies that $\delta B/B_0 \sim \sigma_v/V_A$, where $\delta B$ is the magnitude of a turbulent component of the $B$-field, $B_0$ is the strength of the large-scale $B$-field, $\sigma_v$ is the one-dimensional nonthermal velocity dispersion, and $V_A = B_0/\sqrt{4\pi\rho}$ is the Alfvén speed for a gas with a mass density of $\rho$ (see also Hildebrand et al. 2009). Such a method (the Davis–Chandrasekhar–Fermi method, DCF

method hereafter), in its modified form, has been widely used in estimating the plane-of-sky magnetic field strength $B_{pos}$ from a polarization map by implicitly assuming that $\delta B/B_{pos} \sim \sigma_\theta$, where $\sigma_\theta$ is the measured dispersion of polarization angles about a mean or modeled $B$-field.

Recently, progress has been made toward more accurately quantifying $\delta B/B_{pos}$ from a statistical analysis of polarization angles. In this context, there are different methods based on the

"structure function" (SF) of polarization angles (Hildebrand et al. 2009) or the "autocorrelation function" (ACF) of polarization angles (Houde et al. 2009). Yet another approach is to measure the polarization dispersion with a method analogous to "unsharp masking" (UM; Pattle et al. 2017). Here we use these methods to estimate $B_{pos}$ in Oph-C and compare the results. For the analyses, we use our vector selection criteria of $P/\delta P > 3$ and $\delta P < 5\%$.

In the original version of DCF's field model (Davis 1951; Chandrasekhar & Fermi 1953), the effects of signal integration along the line of sight and across the beam (hereafter beam-integration effect) were not taken into account. Results from theoretical and numerical works have shown that the beam-integration effect can cause the angular dispersion in polarization maps to be underestimated, therefore overestimating the magnetic field strength (Heitsch et al. 2001; Ostriker et al. 2001; Padoan et al. 2001; Falceta-Gonçalves et al. 2008; Houde et al. 2009; Cho & Yoo 2016). To account for this effect, we take a conventional correction factor (we use $Q_c$ to represent this factor throughout this paper) value of 0.5 (Ostriker et al. 2001) to correct the measured angular dispersions and the corresponding magnetic field strength in the SF and UM analyses. The correction parameter $Q_c$ is further discussed in Section 4.3.1.

Assuming the optically thin dust emission, a dust-to-gas ratio $\Lambda$ of 1:100 (Beckwith & Sargent 1991), and an opacity index $\beta$ of 2 (Hildebrand 1983), we calculate gas column density $N(H_2)$ as follows:

$$N(H_2) = \frac{I_\nu}{\mu m_H \kappa_\nu B_\nu(T)}, \qquad (7)$$

where $I_\nu$ is the continuum intensity at frequency $\nu$, $\mu = 2.86$ is the mean molecular weight (Kirk et al. 2013; Pattle et al. 2015), $m_H$ is the atomic mass of hydrogen, $\kappa_\nu = 0.1 (\nu/1 \text{ THz})^\beta$ is the dust opacity (Hildebrand 1983) in cm$^2$ g$^{-1}$, and $B_\nu(T)$ is the Planck function at temperature $T$. In our analyses, we adopted a dust temperature of $10 \pm 3$ K (Stamatellos et al. 2007). The uncertainty on the estimation of column density mainly comes from the uncertainty of $\kappa_\nu$ (Henning et al. 1995). Conservatively, we adopt a fractional uncertainty of 50% (Roy et al. 2014; Pattle et al. 2017) for $\kappa_\nu$. In our calculations, we ignore the uncertainties on $\Lambda$ and $\mu$. The column density was estimated over the area with Stokes $I > 250$ mJy beam$^{-1}$ (see Figure 3). The measured area $A$ is 14,544 arcsec$^2$ (0.0053 pc$^2$). Taking into account the uncertainties on $\kappa_\nu$, temperature, and flux calibration, the fractional uncertainty on the estimated column density is 59%. Therefore, the mean column density in the concerned region is estimated to be $(1.05 \pm 0.62) \times 10^{23}$ cm$^{-2}$. Since the Oph-C core is highly "centrally condensed" (Motte et al. 1998), we adopt a spherical geometry and a core volume ($V$) of $4/3(A^3/\pi)^{1/2}$. Again, we ignore the uncertainty on the geometry assumption. The average volume density $n_{H_2}$ is estimated to be $(6.4 \pm 3.7) \times 10^5$ cm$^{-3}$. The total mass in our measured volume, $M = \mu m_H N(H_2)A$, is $12 \pm 7 \, M_\odot$.

To calculate the plane-of-sky magnetic field strength, we need information about the velocity dispersion of the gas. Assuming isotropic velocity perturbations, we adopt the line-of-sight velocity dispersion estimated by André et al. (2007). In their work, they carried out N$_2$H$^+$ (1–0) observations toward the Ophiuchus main cloud with a 26″ beam using the IRAM

30 m telescope and found that the average line-of-sight nonthermal velocity dispersion, $\sigma_v$, of the dense structures in Oph-C is $0.13 \pm 0.02$ km s$^{-1}$. Their N$_2$H$^+$ data are appropriate to trace the velocity dispersion in Oph-C for many reasons. At 10 K, the critical density of N$_2$H$^+$ (1–0) is $6.1 \times 10^4$ cm$^{-3}$ (Shirley 2015), which is sufficient to probe the dense materials in Oph-C. Also, the masses of dense structures in Oph-C traced by the N$_2$H$^+$ (1–0) data and the SCUBA-2 850 $\mu$m continuum data are in good agreement (Pattle et al. 2015), and the N$_2$H$^+$ (1–0) in Oph-C is optically thin (André et al. 2007), indicating that the N$_2$H$^+$ data and our SCUBA-2/POL-2 data generally trace the same material. Although the beam size of the N$_2$H$^+$ observation is nearly twice the beam size of our POL-2 observation, the spatial resolution of the N$_2$H$^+$ observation, 26″, is still sufficient to resolve the Oph-C core that has a diameter of $\sim 2'$. Thus, it could be concluded that the average line-of-sight nonthermal velocity dispersion of the dense structures in Oph-C traced by N$_2$H$^+$ (1–0) is well suited to represent the average gas motions in our concerned region.

### 3.2.1. SF Analysis

In the SF method (Hildebrand et al. 2009), the magnetic field is assumed to consist of a large-scale structured field, $B_0$, and a turbulent component, $\delta B$. The SF infers the behavior of position angle dispersion as a function of vector separation $l$. At some scale larger than the turbulent scale $\delta$, $\delta B$ should reach its maximum value. At scales smaller than a scale $d$, the higher-order terms of the Taylor expansion of $B_0$ can be canceled out. When $\delta < l \ll d$, the angular dispersion function follows the form

$$\langle \Delta \Phi^2(l) \rangle_{tot} \simeq b^2 + m^2 l^2 + \sigma_M^2(l). \qquad (8)$$

In this equation, $\langle \Delta \Phi^2(l) \rangle_{tot}$, the square of the total measured dispersion function, consists of $b^2$, a constant turbulent contribution, $m^2 l^2$, the contribution from the large-scale structured field, and $\sigma_M^2(l)$, the contribution of the measurement uncertainty. The ratio of the turbulent component and the large-scale component of the magnetic field is given by

$$\frac{\langle \delta B^2 \rangle^{1/2}}{B_0} = \frac{b}{\sqrt{2 - b^2}}, \qquad (9)$$

and $B_0$ is estimated according to

$$B_0 \simeq \sqrt{(2 - b^2) 4\pi \, \mu m_H n_{H_2}} \frac{\sigma_v}{b}. \qquad (10)$$

Then, the estimated plane-of-sky magnetic field strength is corrected by $Q_c$:

$$B_{pos} = Q_c B_0. \qquad (11)$$

Figure 7 shows the angular dispersion corrected by uncertainty ($\langle \Delta \Phi^2(l) \rangle_{tot} - \sigma_M^2(l)$) as a function of distance measured from the polarization map. Following Hildebrand et al. (2009), the data are divided into separate distance bins with separations corresponding to the pixel size. At scales of 0″–25″, the angular dispersion function increases steeply with the segment distance, most possibly due to the contribution of the turbulent field. At scales larger than 25″, the function continues increasing with a shallower slope, which we may attribute to the large-scale ordered magnetic field structure, and reaches its maximum at $\sim 100''$. The maximum of the angular
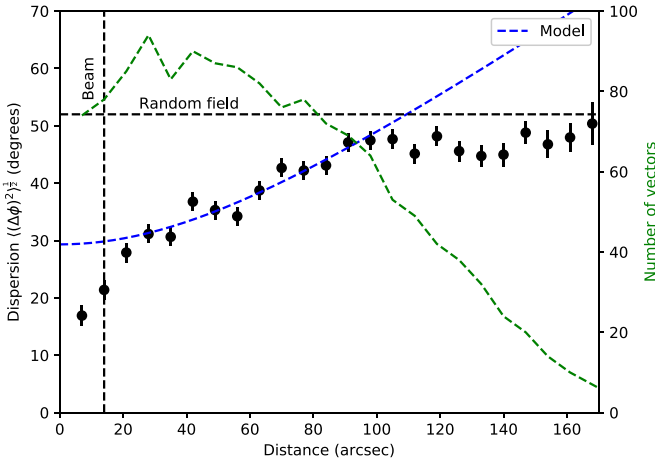
**Figure 7.** Left-hand axis: angular dispersion function for Oph-C. The angle dispersion segments are shown with black filled circles with error bars. The measurement uncertainties were removed. The best fit is shown by the blue dashed line. Right-hand axis: number of independent vectors (green dashed line) included in each data bin. The bin size is $7''$.

dispersion function is lower than the value expected for a random field ($52°$; Poidevin et al. 2010). The angular dispersion function presents wave-like "jitter" features at $l > 25''$. Soler et al. (2016) have attributed the jitter features to the sparse sampling of the vectors in the observed region, which means that the independent vectors involved in each distance bin are not enough to achieve statistical significance. We performed simple Monte Carlo simulations (see the Appendix) and found that the uncertainty from sparse sampling is $\sim1°\!.5$ in the SF for models with SFs similar to that of our data in amounts of large-scale spatial correlation and random angular dispersions. We fit the SF over $25'' < l < 100''$. During the fitting, the uncertainties both from the sparse sampling and from simply propagating the measurement uncertainties of the observed position angles have been taken into account. The reduced chi-squared ($\chi_{red}^2$) of the fitting is 1.2. The calculated values of parameters are given in Table 1 (without correction for the beam-integration effect) and Table 2 (with correction for the beam-integration effect).

### 3.2.2. ACF Analysis

The ACF method (Houde et al. 2009) expands the SF method by including the effect of signal integration along the line of sight and within the beam in the analysis. Houde et al. (2009) write the angular dispersion function in the form

$$1 - \langle \cos[\Delta\Phi(l)]\rangle \simeq \frac{1}{N}\frac{\langle\delta B^2\rangle}{\langle B_0^2\rangle}$$
$$\times [1 - e^{-l^2/2(\delta^2 + 2W^2)}] + a_2' l^2, \quad (12)$$

where $\Delta\Phi(l)$ is the difference in position angles of two vectors separated by a distance $l$, $W$ is the beam radius ($6''\!.0$ for JCMT, i.e., the FWHM beam divided by $\sqrt{8\ln 2}$), $a_2'$ is the slope of the second-order term of the Taylor expansion, and $\delta$ is the turbulent correlation length mentioned before. $N$ is the number of turbulent cells probed by the telescope beam and is given by

$$N = \frac{(\delta^2 + 2W^2)\Delta'}{\sqrt{2\pi}\,\delta^3}, \quad (13)$$

where $\Delta'$ is the effective thickness of the cloud. The ordered magnetic field strength can be derived by

$$B_0 \simeq \sqrt{4\pi\,\mu m_H n_{H_2}}\,\sigma_v \left[\frac{\langle\delta B^2\rangle}{\langle B_0^2\rangle}\right]^{-1/2}. \quad (14)$$

Figure 8(a) shows the angular dispersion function of the polarization segments in the Oph-C region. Figure 8(b) shows the correlated component of the dispersion function. The uncertainty from sparse sampling is $\sim0.015$ in the ACF (see the Appendix). We fit the function at $l < 100''$. Again, the uncertainties both from the sparse sampling and from the measurements have been taken into account. In our fitting, $\Delta'$ is set to $20''$, which is roughly the FWHM of the starless subcore identified by Pattle et al. (2015). The $\chi_{red}^2$ of the fitting is 1.1. The turbulent correlation length $\delta$ is found to be $7''\!.0 \pm 2''\!.7$ ($4.3 \pm 1.6$ mpc). The number of turbulent cells is derived to be $2.5 \pm 0.5$. The calculated values of other parameters are given in Tables 1 and 2.

### 3.2.3. UM Analysis

In this section, we followed Crutcher et al. (2004) to derive the plane-of-sky magnetic field strength with the expression

$$B_{pos} = Q_c \sqrt{4\pi\mu m_H n_{H_2}}\frac{\sigma_v}{\sigma_\theta}. \quad (15)$$

The dispersion of the magnetic field angle, $\sigma_\theta$, is measured following the UM method developed by Pattle et al. (2017). First, a $3 \times 3$ pixel boxcar average is applied to the measured angles to show the local mean field orientation. With a $3 \times 3$ pixel boxcar, the effect of the curvature of the large-scale ordered field on the smoothing is minimized. Then, the deviation in field angle from the mean field orientation is derived by subtracting the smoothed map from the observed magnetic field map. Finally, the standard deviation of the residual angles is measured to represent the angular dispersion of the magnetic field angle.

We applied the UM method to our data and restricted the analysis to pixels where the maximum angle difference within the boxcar is $<90°$. Figure 9 shows the observed position angles $\theta_{obs}$, the position angles $\langle\theta\rangle$ of a mean $B$-field derived by smoothing the observed position angles with a $3 \times 3$ pixel boxcar filter, and the residual values $\theta_{obs} - \langle\theta\rangle$. We then calculated the standard deviation of magnetic field angles ($\sigma_\theta$) as a cumulative function of the maximum permitted angle uncertainty ($\delta\theta_{max}$) in the $3 \times 3$ pixel smoothing box (see Figure 10). With Monte Carlo simulations, Pattle et al. (2017) found that $\sigma_\theta$ can well represent the true angular dispersion when $\delta\theta_{max}$ is small, while $\sigma_\theta$ tend to increase with $\delta\theta_{max}$ when $\delta\theta_{max}$ is large. In our case, we restrict our analysis to $12° < \delta\theta_{max} < 47°$, where $\sigma_\theta$ remains relatively constant within this $\delta\theta_{max}$ range. The average standard deviation is measured to be $10°\!.7 \pm 0°\!.6$ (see Figure 10). This value is introduced in Equation (15) as $\sigma_\theta$. The calculated values of other parameters are given in Tables 1 and 2.

## 4. Discussion

### 4.1. Structure and Orientation of the Magnetic Field

Oph-C is unique in the Ophiuchus cloud, as it is fully a starless core. Investigating the magnetic field structure in starless cores is

**Table 1**
Parameters Derived from Different Modified DCF Methods without Correction for Beam Integration

| Parameter | Description | SF | ACF | UM |
|---|---|---|---|---|
| $\Delta\theta$ (deg) | Angular dispersion | $22 \pm 1$ | $21 \pm 8$ | $11 \pm 1$ |
| $\langle\delta B^2\rangle/\langle B_0^2\rangle$ | Turbulent-to-ordered magnetic field energy ratio | $0.15 \pm 0.01$ | $0.13 \pm 0.10$ | $0.035 \pm 0.004$ |
| $B_{\rm pos}$ ($\mu$G) | Plane-of-sky magnetic field strength | $206 \pm 68$ | $223 \pm 113$ | $426 \pm 141$ |

essential for us to explore the initial conditions of star formation. Previous polarization observations toward cores in the starless phase have shown relatively smooth and uniform magnetic field structures (Ward-Thompson et al. 2000, 2009; Crutcher et al. 2004). Recently, Kandori et al. (2017) presented the first detection of an hourglass-shaped magnetic field in a starless core with NIR polarization observations toward FeSt 1457 (also known as Pipe-109), suggesting that the magnetic field lines can be distorted by mass condensation in the starless phase. However, the NIR polarization observations cannot trace the densest materials in the core, and the hourglass morphology was not found in submillimeter polarization observations toward the same source (Alves et al. 2014). Our observations toward Oph-C, which present the most sensitive submillimeter polarization observation in a low-mass starless core to date, reveal a relatively ordered *B*-field with a prevailing northeast–southwest orientation (see Figure 3). However, the *B*-field structure in Oph-C shows no evidence of an hourglass morphology, which is consistent with previous observations that an hourglass morphology is not generally found in other cold dense cores from submillimeter polarization observations at scales >0.01 pc. This suggests that mass condensation does not significantly distort the local *B*-field structure at scales >0.01 pc in the densest materials of dense cores at both the starless phase and prestellar phase.

The role of magnetic fields in dense cores may vary with the evolution of the core. As part of the BISTRO survey (Ward-Thompson et al. 2017), polarization observations toward two protostellar cores with similar masses (Motte et al. 1998) to that of Oph-C in the Ophiuchus cloud, Oph-A and Oph-B, have been made and are ready to be compared with our data. Our observations of Oph-C show that the overall magnetic field geometry in Oph-C is ordered, and the polarization position angles show large angular dispersions. This behavior is similar to that in Oph-B, which is a relatively quiescent core in Ophiuchus but is more evolved than Oph-C, while the *B*-field in Oph-A, which is the warmest and the only core with substantially gravitationally bound subcores found in Ophiuchus, is mostly well organized and with small angular dispersions (Enoch et al. 2009; Pattle et al. 2015; Kwon et al. 2018; Soam et al. 2018). In addition, the angular dispersions in Oph-C ($\sim 11°$–$22°$) and Oph-B ($\sim 15°$) are larger than those in Oph-A ($\sim 2°$–$6°$). These indicate that the star formation process may reduce angular dispersions in the magnetic field in the late stages of star formation.

Our observations reveal that there is a prevailing orientation in the *B*-field in Oph-C centering at $\sim 40°$–$100°$ (see Figure 5). This orientation agrees with the *B*-field orientations in Oph-A, where the *B*-field components center at $\sim 40°$–$100°$ (Kwon et al. 2018), and Oph-B, where the position angle of *B*-field peaks at $\sim 50°$–$80°$ (Soam et al. 2018). The *B*-field position angle distribution in Oph-C is consistent with the $\sim 50°$ *B*-field component in lower-density regions of the Ophiuchus cloud traced by the NIR polarization map of Kwon et al. (2015), and it is also aligned with the cloud-scale *B*-field orientation

probed by *Planck* (see Figure 3 in Planck Collaboration et al. 2016). The consistency of *B*-field orientation from cloud to core scales indicates that the large-scale magnetic field plays a dominant role in the formation of dense cores in the Ophiuchus cloud.

### 4.2. Depolarization Effect

A clear trend of decreasing polarization percentage with increasing dust emission intensity is seen in Figure 3. Such an effect is more evident in Figure 11(a), in which the *P*–*I* relation suggests depolarization toward high density. Considering that the overall field does not change orientation while threading the core, the depolarization in Oph-C seems unlikely to be a by-product of field tangling of complex small-scale field lines within the JCMT beam. In addition, the subsonic nonthermal gas motions of Oph-C indicate that the polarization percentage has not been significantly affected by the number of turbulent cells along the line of sight. The RAT mechanism (Lazarian 2007), which suggests inefficient grain alignment toward high-density regions, also cannot fully explain the depolarization effect because of the lack of an internal or external radiation field in the Oph-C region. Alternatively, grain characteristics such as size, shape, and composition, which are related to grain alignment mechanism, may explain the depolarization effect. The turbulent structure of the magnetic field, which can induce the field tangling and therefore reduce *P*, also provides a plausible explanation to the decreasing of the polarization percentage toward higher intensities (Planck Collaboration et al. 2015, 2018).

We fitted the *P*–*I* relation with a power-law slope and found that the slope index is $-1.03 \pm 0.05$, which indicates that the polarized intensity is almost constant in Oph-C. The nearly constant polarized intensity is more clearly shown in Figure 11(b). The slope index for Oph-C is slightly lower than the index of $-0.92 \pm 0.05$ for the entire Ophiuchus cloud (Planck Collaboration et al. 2015). For other dense cores in Ophiuchus, a slope index of $-0.7$ to $-0.8$ was found in Oph-A (Kwon et al. 2018), and an index of around $-0.9$ was found in Oph-B (Soam et al. 2018). Considering that Oph-A is the warmest and most evolved among the Oph cores, Oph-B is more quiescent than Oph-A, and Oph-C is the most quiescent region in Ophiuchus (Pattle et al. 2015), it appears that the power-law slope of the *P*–*I* relation is shallower in more evolved dense cores in the Ophiuchus cloud. This trend could be explained by the improved alignment efficiency resulting from the additional internal radiation (predicted by the RAT theory; Lazarian 2007) in more evolved regions. Alternatively, if the depolarization is caused by turbulence (Planck Collaboration et al. 2015, 2018), the stronger turbulence in more evolved dense cores (André et al. 2007) may also be a possible reason for the variation in the slope index. More detailed analysis of the depolarization effect in the Ophiuchus cloud will be presented in a separate publication by the BISTRO team.

**Table 2**
Parameters Derived from Different Modified DCF Methods with Correction for Beam Integration

| Parameter | Description | SF | ACF | UM |
|---|---|---|---|---|
| $\Delta\theta$ (deg) | Angular dispersion | $45 \pm 14$ | $34 \pm 13$ | $21 \pm 7$ |
| $\langle\delta B^2\rangle/\langle B_0^2\rangle$ | Turbulent-to-ordered magnetic field energy ratio | $0.61 \pm 0.37$ | $0.35 \pm 0.27$ | $0.14 \pm 0.09$ |
| $B_{pos}$ ($\mu$G) | Plane-of-sky magnetic field strength | $103 \pm 46$ | $136 \pm 69$ | $213 \pm 115$ |
| $\lambda$ | Observed magnetic stability critical parameter | $7.8 \pm 5.7$ | $5.9 \pm 4.6$ | $3.8 \pm 3.0$ |
| $\lambda_c$ | Corrected magnetic stability critical parameter | $2.6 \pm 1.9$ | $1.9 \pm 1.5$ | $1.3 \pm 1.0$ |
| $E_B$ ($10^{35}$ J) | Total magnetic energy | $5.4 \pm 4.8$ | $9.5 \pm 9.7$ | $23.2 \pm 25.0$ |
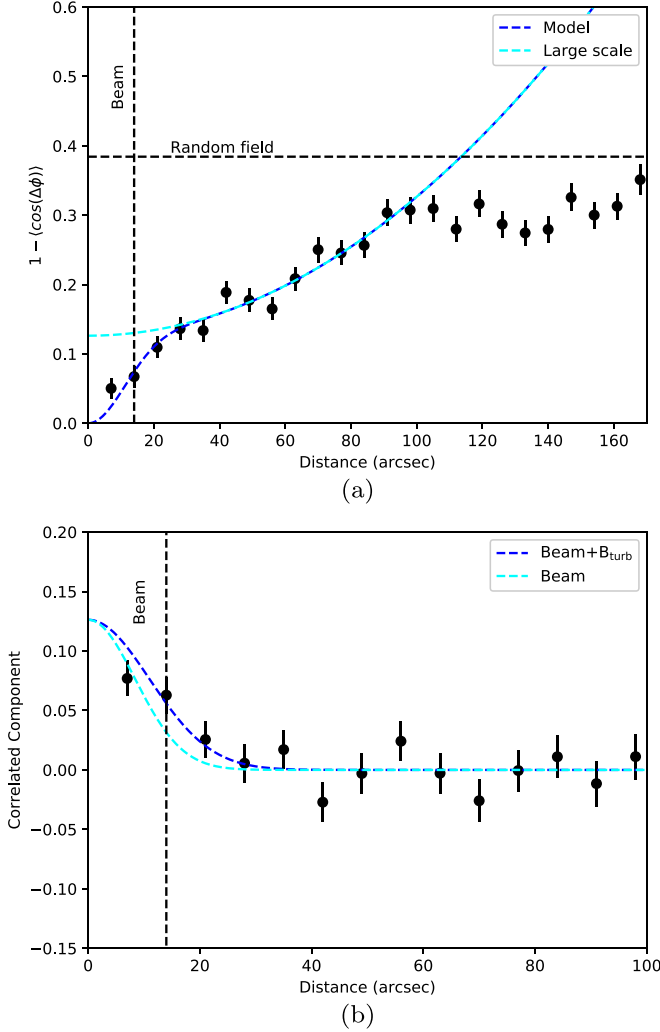


**Figure 8.** (a) Angular dispersion function for Oph-C. The angle dispersion segments are shown with black filled circles with error bars. The bin size is the same as that in Figure 7. A blue dashed line shows the fitted dispersion function. The cyan dashed line shows the large-scale component $(1/N)(\langle\delta B^2\rangle/\langle B_0^2\rangle) + a_2' l^2$ of the best fit. (b) Correlated component of the dispersion function. The correlated component $(1/N)\langle\delta B^2\rangle/\langle B_0^2\rangle)e^{-l^2/2(\delta^2+2W^2)}$ is shown with a blue dashed line. The cyan dashed line shows the correlated component solely due to the beam.

## 4.3. Magnetic Field Strength

### 4.3.1. Comparison of Three Modified DCF Methods

While the morphologies of magnetic fields can help us to qualitatively understand its role in the star formation process, the magnetic field strength is important in quantitatively assessing the significance of the magnetic field compared to gravity based on the mass-to-flux ratio, and compared to turbulence based on the ratio of random to ordered components in polarization angle statistics. The strengths of magnetic fields, however, cannot be measured directly from polarization observations. In this paper, we estimated the average magnetic field strength in Oph-C from different modified DCF methods. Results of these methods are shown in Tables 1 and 2. From the statistical analyses of the dispersion of dust polarization angles, the beam-integrated angular dispersions derived from the SF and ACF methods are consistent with each other ($\sim 21°$–$22°$) and are larger than that derived from the UM method ($\sim 11°$), indicating that the magnetic field strength estimated from the UM method could be systematically larger than that derived from the SF method and the ACF method. Similar behavior was found when applying these methods on the polarization map of OMC-1 (Hildebrand et al. 2009; Houde et al. 2009; Pattle et al. 2017), a region that has a relatively stronger magnetic field (the $B_{pos}$ is $\sim 13.2$ mG estimated from the UM method and $\sim 3.5$–$3.8$ mG estimated from the SF/ACF method without correction for beam integration) than that in Oph-C. The estimated $B_{pos}$ in Oph-C ($\sim 0.1$–$0.2$ mG) is lower than that in Oph-A ($\sim 0.2$–$5$ mG) and Oph-B ($\sim 0.6$ mG).

Because the results of the dispersion function analysis could be affected by the bin size (Koch et al. 2010), we have redone the SF and ACF analyses to find the dependence on the bin size. We found that oversampling (with bin size $<7''$) would inject additional noises into the dispersion functions (both SF and ACF), thus leading to overestimation of the angular dispersion and underestimation of the $B$-field strength. The origin of the additional noise is possibly related to the wrongly generated masks, due to small pixel size in the POL-2 data reduction process, and needs to be further investigated. Increasing the bin size, on the other hand, shows little effect on the SF method and leads to larger values of turbulent scale and $B$-field strength for the results of the ACF method. We also found that, by undersampling, the turbulent scale estimated from the ACF method is always approximately equal to the bin size. The effects on the ACF method can be simply explained by a loss of information on small scales due to undersampling. Koch et al. (2010) have also investigated the dependence of the SF method on the bin size but got different results from ours: oversampling shows little effect on the SF, while undersampling biases the analysis toward larger dispersion values. This indicates that the dependence of dispersion function on the bin size is not simple. Considering these factors and that the derived turbulent scale ($\sim 7''.0$) is approximately equal to the Nyquist sampling interval of our data, we note that the turbulent scale along with the $B$-field strength derived from the ACF method could be overestimated.

Increasing the box size for smoothing would significantly overestimate the angular dispersion derived from the UM method because of field curvature, while in a zero-curvature
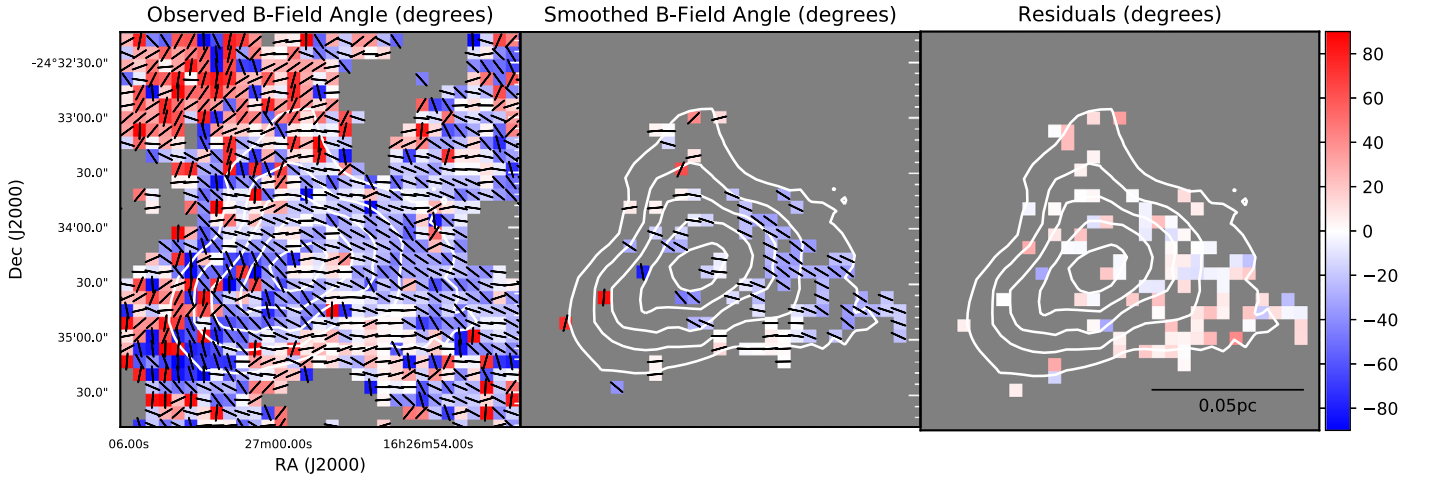
**Figure 9.** Left panel: observed magnetic field angles $\theta_{\mathrm{obs}}$. Middle panel: smoothed magnetic field angles $\langle\theta\rangle$. Right panel: residual angles $\theta_{\mathrm{obs}} - \langle\theta\rangle$. The vectors are of uniform length. The angles are measured south of east so that the color bars of the observed, smoothed, and residual angles are unified.
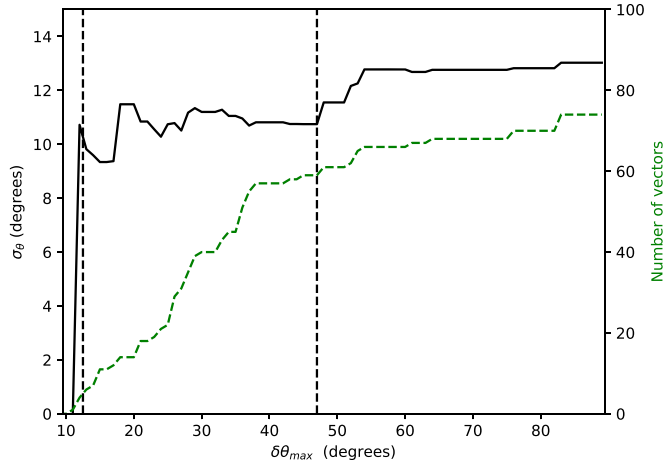


**Figure 10.** Left-hand axis: $\sigma_\theta$ as a cumulative function of $\delta\theta_{\mathrm{max}}$, shown by the black solid line. Right-hand axis: number of vectors (green dashed line) included in the cumulative function. The average standard deviation is measured over the region between two black dashed lines.

case decreasing the box size would slightly underestimate the angular dispersion (Pattle et al. 2017). Since the $B$-field in Oph-C does not show well-defined shapes, it is unclear whether the angular dispersion in Oph-C is underestimated or overestimated by the UM method. We checked the dependence on the box size in our UM analysis by reapplying the UM method to our data with a $5 \times 5$ pixel smoothing box and a $7 \times 7$ pixel smoothing box and derived angular dispersions of $\sim 11°-12°$, indicating that a larger smoothing box would not significantly change the results of our UM analysis.

Systematic uncertainties of the DCF method may arise from the beam-integration effect. For the UM method and the SF method, we use a correction factor $Q_c$ to account for the averaging effect of turbulent cells along the line of sight. Ostriker et al. (2001) found that $Q_c$ is in the range of 0.46–0.51 for angular dispersions less than 25°. In our case, the Gaussian fitting of the position angles of polarization segments in Oph-C gives a standard deviation of angle of 33°, which is larger than the angular dispersion limit of Ostriker et al. (2001). However, this standard deviation includes the contribution from the curvature of the large-scale field. Excluding
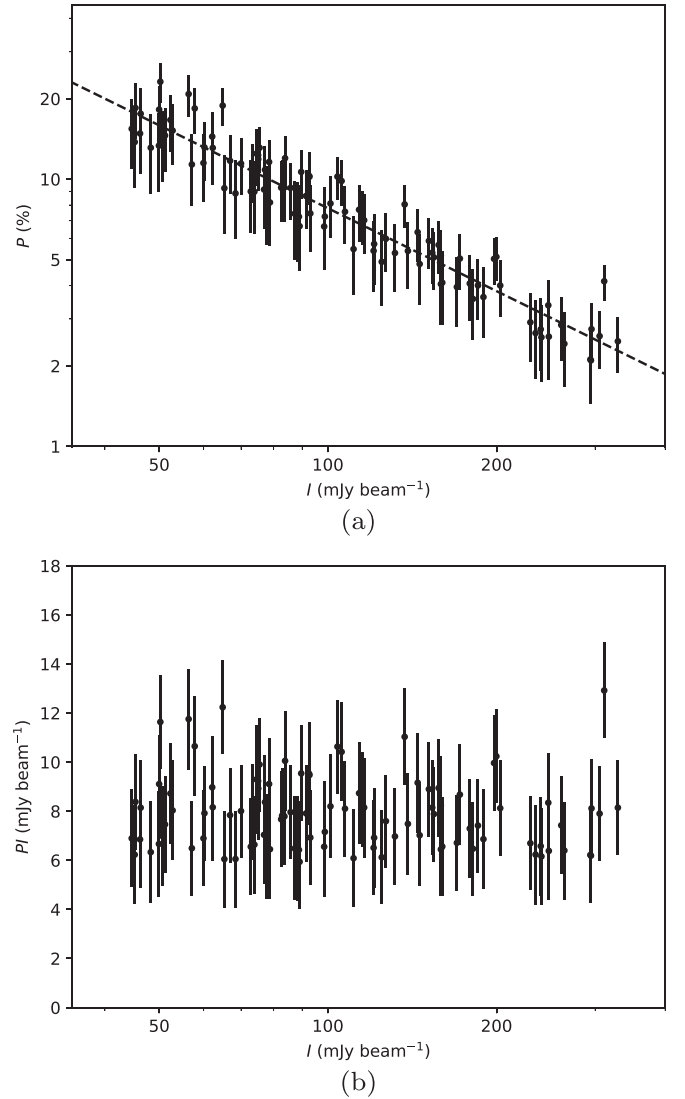




**Figure 11.** (a) Polarization degree vs. total intensity. (b) Polarized intensity vs. total intensity. Data points with $P/\delta P > 3$ and $\delta P < 5\%$ are shown with error bars. The result of the power-law fitting of the $P$–$I$ relation is shown by the dashed line.

the angular variations of the large-scale field, we got standard deviations $<25°$ from the modified DCF methods. Hence, we adopted a conventional $Q_c$ value of 0.5. The uncertainty of the $Q_c$ value is $\sim30\%$ (Crutcher et al. 2004). On the other hand, the ACF method takes into account the beam-integration effect by directly fitting the angular dispersion function. The number of turbulent cells of $\sim2.5$ derived from the ACF method is equivalent to a $Q_c$ of $\sim0.63$, which is slightly larger than the correlation factor adopted by the SF analysis and the UM analysis.

As mentioned by Crutcher (2012), even applying the most complicated modified DCF method on the highest-quality data would lead to a $B_{pos}$ value with an uncertainty varying by a factor of two or more, for various reasons. It is essential to assess the accuracy of these methods by comparing the results of these methods on polarization maps from simulations. Although the magnetic field strengths estimated from the three modified DCF methods may have systematic differences, they are consistent with each other within the uncertainties, indicating that these results are robust to some extent, and that we can still compare the relative importance of magnetic field with gravity and turbulence with these results.

### 4.3.2. Magnetic Field versus Gravity

To find out whether or not the magnetic field can support Oph-C against gravity, we compared the ratio of mass to magnetic flux with the critical ratio using the local magnetic stability critical parameter $\lambda$ (Crutcher et al. 2004):

$$\lambda = \frac{(M/\Phi)_{observed}}{(M/\Phi)_{critical}}, \tag{16}$$

where $(M/\Phi)_{observed}$ is the observed ratio of mass to magnetic flux,

$$\left(\frac{M}{\Phi}\right)_{observed} = \frac{\mu m_H N(H_2)}{B}, \tag{17}$$

and $(M/\Phi)_{critical}$ is the critical ratio of mass to magnetic flux,

$$\left(\frac{M}{\Phi}\right)_{critical} = \frac{1}{2\pi\sqrt{G}}. \tag{18}$$

We estimated $\lambda$ using the relation in Crutcher et al. (2004):

$$\lambda = 7.6 \times 10^{-21} \frac{N(H_2)}{B_{pos}}. \tag{19}$$

The observed critical parameters derived from the SF, ACF, and UM methods are $7.8 \pm 5.7$, $5.9 \pm 4.6$, and $3.8 \pm 3.0$ (see Table 2), respectively. Crutcher et al. (2004) proposed that the observed $M/\phi$ along with $\lambda$ are overestimated because of geometrical effects. Crutcher et al. (1993) found an average line-of-sight $B$-field strength ($B_{los}$) of $6.8 \pm 2.5\ \mu G$ in the Ophiuchus cloud based on OH Zeeman observations with an $18'$ beam. Their estimated $B_{los}$ is much smaller than the $B_{pos}$ inferred by our analyses, indicating that the $B$-field in Oph-C is possibly lying near the plane of the sky. However, since quasi-thermal OH emissions cannot trace high-density materials with $n(H_2) > 10^4\ cm^{-3}$ and the beam of the OH Zeeman observation is much larger than that of our polarization maps, it is more likely that the line-of-sight $B$-field strength in the Oph-C is underestimated by Crutcher et al. (1993). As the degree of the underestimation of $B_{los}$ is unknown, the correction factor for the geometrical bias cannot be derived by simply comparing $B_{los}$ and $B_{pos}$. Alternatively, we adopted a statistical correction

factor of 3 (Crutcher et al. 2004). By applying this correction, we obtain corrected critical parameters ($\lambda_c$) of $2.6 \pm 1.9$, $1.9 \pm 1.5$, and $1.3 \pm 1.0$ (see Table 2) for the SF, ACF, and UM methods, respectively. These values indicate that the Oph-C region is near magnetically critical or slightly magnetically supercritical (i.e., unstable to collapse).

### 4.3.3. Magnetic Field versus Turbulence

To compare the relative importance of the magnetic field and turbulence in Oph-C, we calculated the magnetic field energy and the internal nonthermal kinetic energy. The total magnetic field energy is given by

$$E_B = \frac{B^2 V}{2\mu_0} \tag{20}$$

in SI units, where $\mu_0$ is the permeability of vacuum and $B = \frac{4}{\pi} B_{pos}$ (Crutcher et al. 2004) is the total magnetic field strength. The internal nonthermal kinetic energy is derived by

$$E_{K,NT} = \frac{3M\sigma_v^2}{2}. \tag{21}$$

For the estimated volume (see Section 3.2) of Oph-C, the internal nonthermal kinetic energy is $(6.1 \pm 2.0) \times 10^{35}$ J. The total magnetic field energy measured from the SF, ACF, and UM methods is $(5.4 \pm 4.8) \times 10^{35}$ J, $(9.5 \pm 9.7) \times 10^{35}$ J, and $(2.3 \pm 2.5) \times 10^{36}$ J (see Table 2), respectively. The $E_B$ calculated from the SF method is comparable to $E_{K,NT}$, while the values of $E_B$ estimated from the ACF and UM methods are greater than $E_{K,NT}$. However, the uncertainty is more than 100% for the values of $E_B$ calculated from the ACF and UM methods. Thus, we can only set upper limits for the total magnetic field energy in Oph-C from these two methods.

## 5. Summary

As part of the BISTRO survey, we have presented the $850\ \mu m$ polarization observations toward the Oph-C region with the POL-2 instrument at the JCMT. The main conclusions of this work are as follows:

1. Our POL-2 observations are much more sensitive and trace a larger area than previous SCUPOL observations. Unlike the randomly distributed magnetic field orientations traced by the SCUPOL observations, the magnetic field traced by our POL-2 observations shows an ordered field geometry with a predominant orientation of northeast–southwest. We found the average angular difference of spatially over-lapping vectors between the two data sets to be $\sim39°$. We performed a K-S test on the position angles and found that the POL-2 data and the SCUPOL data have low probability (0.06) to be drawn from the same distribution. The inconsistency between the POL-2 and the SCUPOL data may be explained by the low S/N of the SCUPOL data.

2. The $B$-field orientation in Oph-C is consistent with the $B$-field orientations in Oph-A and Oph-B. The orientation also agrees with the $B$-field component in lower-density regions traced by NIR observations and is aligned with the cloud-scale $B$-field orientation revealed by *Planck*.

3. We detect a decreasing polarization percentage as a function of increasing total intensity in the Oph-C region. The power-law slope index is found to be $-1.03 \pm 0.05$,

suggesting that the polarized intensity is almost constant in Oph-C.

4. We compare the plane-of-sky magnetic field strength in Oph-C calculated from different modified DCF methods. The $B_{pos}$ calculated by the SF method, the ACF method, and the UM method are $103 \pm 46\,\mu G$, $136 \pm 69\,\mu G$, and $213 \pm 115\,\mu G$, respectively.

5. The ratio of mass to magnetic flux of Oph-C is found to be comparable to or slightly higher than its critical value, suggesting that the Oph-C region is near magnetically critical or magnetically supercritical (i.e., unstable to collapse).

6. In Oph-C, the total magnetic energy calculated from the SF method is comparable to the turbulent energy. Due to large uncertainties, the ACF method and the UM method only set upper limits for the total magnetic energy.

7. We compared our work with studies of two other dense cores in the Ophiuchus cloud. We find that the $B$-fields in Oph-C and Oph-B have larger angular dispersions than Oph-A. We also find a possible trend of shallower $P$–$I$ relationship with evolution in the three dense cores in the Ophiuchus region. In addition, the $B_{pos}$ in Oph-C is lower than $B_{pos}$ of more evolved regions (e.g., Oph-A and Oph-B) in Ophiuchus.

## Appendix
## Uncertainty from Sparse Sampling

Here we derive the uncertainty in the dispersion function caused by the lack of vector samples (sparse sampling). We perform simple Monte Carlo simulations of modeled structured fields with randomly generated Gaussian dispersions to roughly estimate the uncertainty of sparse sampling in the dispersion function of our data. It should be noted that because simulating the beam-integration effect is extremely time-consuming and only affects the first two or three data points of the dispersion function, the beam-integration effect is not taken into account in our toy models.

We start with generating the underlying field model. We note that since the uncertainty in the angular dispersion function due to sparse sampling is only related to the amount of spatial correlation of field orientations across the sky and the amount of angular dispersion relative to the structured field (Soler et al. 2016), the choice of the underlying field model is arbitrary. We build a set of underlying parabola models (e.g., Girart et al. 2006; Rao et al. 2009; Qiu et al. 2014) with the form

$$y = g + gCx^2, \tag{22}$$

where $x$ is the offsets in pixels along the field axis from the center of symmetry. In Figures 12(a) and (b), a parabola field model with $C = 0.13$ is shown in magenta curves as an example.

We then derive the orientation of the modeled sparsely sampled $B$-vectors by applying a Gaussian angular dispersion of $22°$ (to match the angular dispersion of $\sim 21°$–$22°$ derived from the SF and ACF methods) to the underlying $B$-vectors with the same spatial distributions as those of the observed $B$-vectors in Oph-C with $P/\delta P > 3$ and $\delta P < 5\%$, while the offsets and angle of the modeled $B$-vectors with respect to the center of symmetry of the underlying modeled field are random. An example of the modeled sparsely sampled $B$-vectors is shown in Figure 12(a).

In a similar way, we also derived the orientation of "unbiased" samples of $B$-vectors with a Gaussian angular dispersion of $22°$ and spatial separation of 1 pixel ($7''$) for comparison. There are enough vectors in the "unbiased" sample to achieve statistical significance. An example of the modeled "unbiased" $B$-vectors is shown in Figure 12(b).

We calculate the SF and ACF (see Figures 12(c) and (d) for examples of the SF and ACF) from the sparse samples and "unbiased" samples of modeled vectors and find that the average deviations of the SFs and ACFs between the two sets of samples are $\sim 1°.5$ and $\sim 0.015$ over $25'' < l < 100''$, relatively for SFs and ACFs with similar amounts of large-scale spatial correlation and random angular dispersions (e.g., similar SF and ACF shapes over $25'' < l < 100''$) to the dispersion functions calculated from the observed data. These average deviations, which are larger than the statistical uncertainties ($\sim 0°.6$ for the SF and $\sim 0.007$ for the ACF over $25'' < l < 100''$ in average) propagated from the measurement uncertainty, are introduced in our analyses as the uncertainties due to sparse sampling.
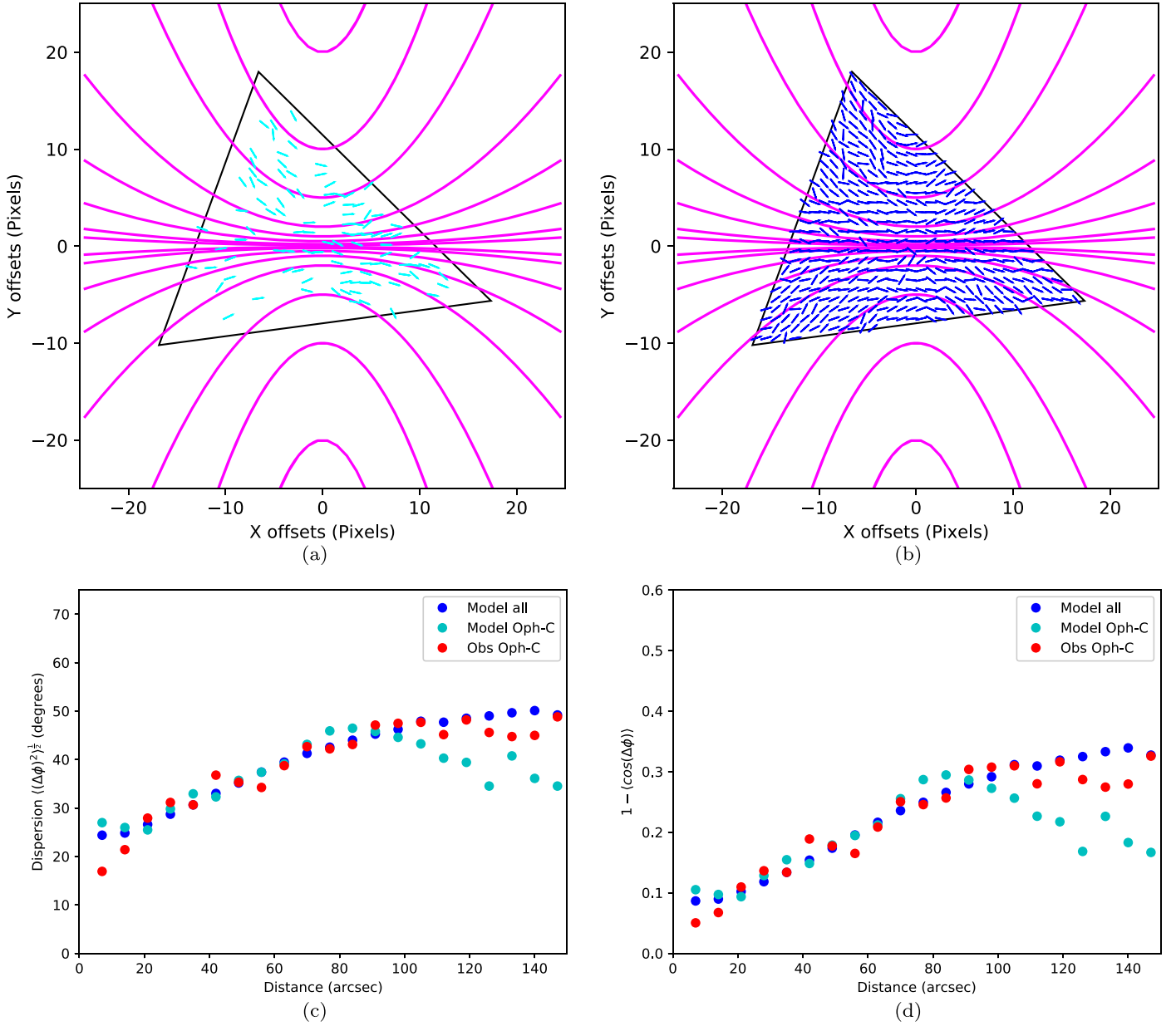
**Figure 12.** (a) Modeled sparsely sampled *B*-vectors with an angular dispersion of 22° are shown in cyan. (b) Modeled "unbiased" *B*-vectors with an angular dispersion of 22° are shown in blue. In panels (a) and (b), magenta curves denote the underlying parabola field models with $C = 0.13$. Vectors are of unit length. The triangle marks the region in which we calculated the "unbiased" dispersion function. (c) SFs calculated from samples corresponding to all modeled vectors in the triangle region (blue), modeled Oph-C vectors (cyan), and observed Oph-C vectors (red). (d) ACF, with the same symbols as those in panel (c).

## ORCID iDs

Junhao Liu ⓘ https://orcid.org/0000-0002-4774-2998
Keping Qiu ⓘ https://orcid.org/0000-0002-5093-5088
James Di Francesco ⓘ https://orcid.org/0000-0002-9289-2450
Pierre Bastien ⓘ https://orcid.org/0000-0002-0794-3859
Patrick M. Koch ⓘ https://orcid.org/0000-0003-2777-5861
Ray S. Furuya ⓘ https://orcid.org/0000-0003-0646-8782
Kee-Tae Kim ⓘ https://orcid.org/0000-0003-2412-7092
Simon Coudé ⓘ https://orcid.org/0000-0002-0859-0805
Chang Won Lee ⓘ https://orcid.org/0000-0002-3179-6334
Archana Soam ⓘ https://orcid.org/0000-0002-6386-2906
Chakali Eswaraiah ⓘ https://orcid.org/0000-0003-4761-6139
Di Li ⓘ https://orcid.org/0000-0003-3010-7661
A-Ran Lyo ⓘ https://orcid.org/0000-0002-9907-8427
Kate Pattle ⓘ https://orcid.org/0000-0002-8557-3582

Woojin Kwon ⓘ https://orcid.org/0000-0003-4022-4132
Shih-Ping Lai ⓘ https://orcid.org/0000-0001-5522-486X
Derek Ward-Thompson ⓘ https://orcid.org/0000-0003-1140-2761
Tao-Chung Ching ⓘ https://orcid.org/0000-0001-8516-2532
Qilao Gu ⓘ https://orcid.org/0000-0002-2826-1902
Hua-bai Li ⓘ https://orcid.org/0000-0003-2641-9240
Lei Qian ⓘ https://orcid.org/0000-0003-0597-0957
Hongchi Wang ⓘ https://orcid.org/0000-0003-0746-7968
Jinghua Yuan ⓘ https://orcid.org/0000-0001-8060-3538
Chuan-Peng Zhang ⓘ https://orcid.org/0000-0002-4428-3183
Yusuke Aso ⓘ https://orcid.org/0000-0002-8238-7709
Do-Young Byun ⓘ https://orcid.org/0000-0003-1157-4109
Michael Chun-Yuan Chen ⓘ https://orcid.org/0000-0002-9774-1846

Wen Ping Chen ⓘ https://orcid.org/0000-0003-0262-272X
Jungyeon Cho ⓘ https://orcid.org/0000-0003-1725-4376
Antonio Chrysostomou ⓘ https://orcid.org/0000-0002-9583-8644
Eun Jung Chung ⓘ https://orcid.org/0000-0003-0014-1527
Stewart P. S. Eyres ⓘ https://orcid.org/0000-0002-6663-7675
Rachel K. Friesen ⓘ https://orcid.org/0000-0001-7594-8128
Gary Fuller ⓘ https://orcid.org/0000-0001-8509-1818
Tim Gledhill ⓘ https://orcid.org/0000-0002-2859-4600
Sarah F. Graves ⓘ https://orcid.org/0000-0001-9361-5781
Jane S. Greaves ⓘ https://orcid.org/0000-0002-3133-413X
Jennifer Hatchell ⓘ https://orcid.org/0000-0002-4870-2760
Thiem Hoang ⓘ https://orcid.org/0000-0003-2017-0982
Martin Houde ⓘ https://orcid.org/0000-0003-4420-8674
Shu-ichiro Inutsuka ⓘ https://orcid.org/0000-0003-4366-6518
Kazunari Iwasaki ⓘ https://orcid.org/0000-0002-2707-7548
Doug Johnstone ⓘ https://orcid.org/0000-0002-6773-459X
Ji-hyun Kang ⓘ https://orcid.org/0000-0001-7379-6263
Miju Kang ⓘ https://orcid.org/0000-0002-5016-050X
Sung-ju Kang ⓘ https://orcid.org/0000-0002-5004-7216
Akimasa Kataoka ⓘ https://orcid.org/0000-0003-4562-4119
Koji S. Kawabata ⓘ https://orcid.org/0000-0001-6099-9539
Gwanjeong Kim ⓘ https://orcid.org/0000-0003-2011-8172
Kyoung Hee Kim ⓘ https://orcid.org/0000-0001-9597-7196
Mi-Ryang Kim ⓘ https://orcid.org/0000-0002-1408-7747
Shinyoung Kim ⓘ https://orcid.org/0000-00001-9333-5608
Jason M. Kirk ⓘ https://orcid.org/0000-0002-4552-7477
Masato I. N. Kobayashi ⓘ https://orcid.org/0000-0003-3990-1204
Takayoshi Kusune ⓘ https://orcid.org/0000-0002-9218-9319
Jungmi Kwon ⓘ https://orcid.org/0000-0003-2815-7774
Kevin M. Lacaille ⓘ https://orcid.org/0000-0001-9870-5663
Chin-Fei Lee ⓘ https://orcid.org/0000-0002-3024-5864
Jeong-Eun Lee ⓘ https://orcid.org/0000-0003-3119-2087
Hyeseung Lee ⓘ https://orcid.org/0000-0003-3465-3213
Sang-Sung Lee ⓘ https://orcid.org/0000-0002-6269-594X
Sheng-Yuan Liu ⓘ https://orcid.org/0000-0003-4603-7119
Tie Liu ⓘ https://orcid.org/0000-0002-5286-2564
Sven van Loo ⓘ https://orcid.org/0000-0003-4746-8500
Steve Mairs ⓘ https://orcid.org/0000-0002-6956-0730
Brenda C. Matthews ⓘ https://orcid.org/0000-0003-3017-9577
Gerald H. Moriarty-Schieven ⓘ https://orcid.org/0000-0002-0393-7822
Fumitaka Nakamura ⓘ https://orcid.org/0000-0001-5431-2294
Nagayoshi Ohashi ⓘ https://orcid.org/0000-0003-0998-5064
Takashi Onaka ⓘ https://orcid.org/0000-0002-8234-6747
Harriet Parsons ⓘ https://orcid.org/0000-0002-6327-3423
Andy Pon ⓘ https://orcid.org/0000-0003-4612-1812
Tae-Soo Pyo ⓘ https://orcid.org/0000-0002-3273-0804
Ramprasad Rao ⓘ https://orcid.org/0000-0002-1407-7944
Mark G. Rawlings ⓘ https://orcid.org/0000-0002-6529-202X
John Richer ⓘ https://orcid.org/0000-0002-9693-6860
Sarah Sadavoy ⓘ https://orcid.org/0000-0001-7474-6874
Anna M. M. Scaife ⓘ https://orcid.org/0000-0002-5364-2301
Hiroko Shinnaga ⓘ https://orcid.org/0000-0001-9407-6775
Motohide Tamura ⓘ https://orcid.org/0000-0002-6510-0681
Ya-Wen Tang ⓘ https://orcid.org/0000-0002-0675-276X
Kohji Tomisaka ⓘ https://orcid.org/0000-0003-2726-0892
Yusuke Tsukamoto ⓘ https://orcid.org/0000-0001-6738-676X

Jia-Wei Wang ⓘ https://orcid.org/0000-0002-6668-974X
Hsi-Wei Yen ⓘ https://orcid.org/0000-0003-1412-893X
Hyunju Yoo ⓘ https://orcid.org/0000-0002-8578-1728

## References

Alves, F. O., Frau, P., Girart, J. M., et al. 2014, A&A, 569, L1
André, P., Belloche, A., Motte, F., & Peretto, N. 2007, A&A, 472, 519
Astropy Collaboration, Robitaille, T. P., Tollerud, E. J., et al. 2013, A&A, 558, A33
Beckwith, S. V. W., & Sargent, A. I. 1991, ApJ, 381, 250
Berry, D. S., Gledhill, T. M., Greaves, J. S., & Jenness, T. 2005, in ASP Conf. Ser. 343, Astronomical Polarimetry: Current Status and Future Directions, ed. A. Adamson et al. (San Francisco, CA: ASP), 71
Chandrasekhar, S., & Fermi, E. 1953, ApJ, 118, 113
Chapin, E., Gibb, A. G., Jenness, T., et al. 2013, StaUN, 258
Cho, J., & Yoo, H. 2016, ApJ, 821, 21
Crutcher, R. M. 2012, ARA&A, 50, 29
Crutcher, R. M., Nutter, D. J., Ward-Thompson, D., & Kirk, J. M. 2004, ApJ, 600, 279
Crutcher, R. M., Troland, T. H., Goodman, A. A., et al. 1993, ApJ, 407, 175
Currie, M. J., Berry, D. S., Jenness, T., et al. 2014, adass XXIII, 485, 391
Davis, L. 1951, PhRv, 81, 890
Dempsey, J. T., Friberg, P., Jenness, T., et al. 2013, MNRAS, 430, 2534
Dotson, J. L., Vaillancourt, J. E., Kirby, L., et al. 2010, ApJS, 186, 406
Enoch, M. L., Evans, N. J., II, Sargent, A. I., & Glenn, J. 2009, ApJ, 692, 973
Falceta-Gonçalves, D., Lazarian, A., & Kowal, G. 2008, ApJ, 679, 537
Friberg, P., Bastien, P., Berry, D., et al. 2016, Proc. SPIE, 9914, 991403
Galli, D., & Shu, F. H. 1993a, ApJ, 417, 220
Galli, D., & Shu, F. H. 1993b, ApJ, 417, 243
Girart, J. M., Beltrán, M. T., Zhang, Q., Rao, R., & Estalella, R. 2009, Sci, 324, 1408
Girart, J. M., Crutcher, R. M., & Rao, R. 1999, ApJL, 525, L109
Girart, J. M., Rao, R., & Marrone, D. P. 2006, Sci, 313, 812
Hall, J. S. 1949, Sci, 109, 166
Heitsch, F., Zweibel, E. G., Mac Low, M.-M., Li, P., & Norman, M. L. 2001, ApJ, 561, 800
Henning, T., Michel, B., & Stognienko, R. 1995, P&SS, 43, 1333
Hildebrand, R. H. 1983, QJRAS, 24, 267
Hildebrand, R. H. 1988a, ApL&C, 26, 263
Hildebrand, R. H. 1988b, QJRAS, 29, 327
Hildebrand, R. H., Kirby, L., Dotson, J. L., Houde, M., & Vaillancourt, J. E. 2009, ApJ, 696, 567
Hiltner, W. A. 1949, Sci, 109, 165
Holland, W. S., Bintley, D., Chapin, E. L., et al. 2013, MNRAS, 430, 2513
Houde, M., Vaillancourt, J. E., Hildebrand, R. H., Chitsazzadeh, S., & Kirby, L. 2009, ApJ, 706, 1504
Hull, C. L. H., Mocz, P., Burkhart, B., et al. 2017, ApJL, 842, L9
Hull, C. L. H., Plambeck, R. L., Kwon, W., et al. 2014, ApJS, 213, 13
Hunter, J. D. 2007, CSE, 9, 90
Jenness, T., Chapin, E. L., Berry, D. S., et al. 2013, SMURF: SubMillimeter User Reduction Facility, Astrophysics Source Code Library, ascl:1310.007
Kandori, R., Tamura, M., Kusakabe, N., et al. 2017, ApJ, 845, 32
Kirk, J. M., Ward-Thompson, D., Palmeirim, P., et al. 2013, MNRAS, 432, 1424
Koch, P. M., Tang, Y.-W., & Ho, P. T. P. 2010, ApJ, 721, 815
Kwon, J., Doi, Y., Tamura, M., et al. 2018, ApJ, 859, 4
Kwon, J., Tamura, M., Hough, J. H., et al. 2015, ApJS, 220, 17
Lazarian, A. 2007, JQSRT, 106, 225
Lazarian, A., & Hoang, T. 2007, MNRAS, 378, 910
Loren, R. B., Wootten, A., & Wilking, B. A. 1990, ApJ, 365, 269
Mac Low, M.-M., & Klessen, R. S. 2004, RvMP, 76, 125
Matthews, B. C., McPhee, C. A., Fissel, L. M., & Curran, R. L. 2009, ApJS, 182, 143
Motte, F., Andre, P., & Neri, R. 1998, A&A, 336, 150
Mouschovias, T. C., Tassis, K., & Kunz, M. W. 2006, ApJ, 646, 1043
Naghizadeh-Khouei, J., & Clarke, D. 1993, A&A, 274, 968
Ortiz-León, G. N., Loinard, L., Kounkel, M. A., et al. 2017, ApJ, 834, 141
Ossenkopf, V., & Henning, T. 1994, A&A, 291, 943
Ostriker, E. C., Stone, J. M., & Gammie, C. F. 2001, ApJ, 546, 980
Padoan, P., Federrath, C., Chabrier, G., et al. 2014, in Protostars and Planets VI, ed. H. Beuther et al. (Tucson, AZ: Univ. Arizona Press), 77
Padoan, P., Goodman, A., Draine, B. T., et al. 2001, ApJ, 559, 1005
Pattle, K., Ward-Thompson, D., Berry, D., et al. 2017, ApJ, 846, 122

Pattle, K., Ward-Thompson, D., Hasegawa, T., et al. 2018, ApJL, 860, L6
Pattle, K., Ward-Thompson, D., Kirk, J. M., et al. 2015, MNRAS, 450, 1094
Planck Collaboration, Ade, P. A. R., Aghanim, N., et al. 2015, A&A, 576, A105
Planck Collaboration, Ade, P. A. R., Aghanim, N., et al. 2016, A&A, 586, A138
Planck Collaboration, Aghanim, N., Akrami, Y., et al. 2018, arXiv:1807.06212
Poidevin, F., Bastien, P., & Matthews, B. C. 2010, ApJ, 716, 893
Qiu, K., Zhang, Q., Menten, K. M., et al. 2014, ApJL, 794, L18
Rao, R., Girart, J. M., Marrone, D. P., Lai, S.-P., & Schnee, S. 2009, ApJ, 707, 921
Robitaille, T., & Bressert, E. 2012, APLpy: Astronomical Plotting Library in Python, Astrophysics Source Code Library, ascl:1208.017
Roy, A., André, P., Palmeirim, P., et al. 2014, A&A, 562, A138
Santos, F. P., Franco, G. A. P., Roman-Lopes, A., Reis, W., & Román-Zúñiga, C. G. 2014, ApJ, 783, 1
Shirley, Y. L. 2015, PASP, 127, 299
Soam, A., Pattle, K., Ward-Thompson, D., et al. 2018, ApJ, 861, 65
Soler, J. D., Alves, F., Boulanger, F., et al. 2016, A&A, 596, A93
Soler, J. D., Hennebelle, P., Martin, P. G., et al. 2013, ApJ, 774, 128
Stamatellos, D., Whitworth, A. P., & Ward-Thompson, D. 2007, MNRAS, 379, 1390
Stephens, I. W., Looney, L. W., Kwon, W., et al. 2013, ApJL, 769, L15
Vaillancourt, J. E. 2006, PASP, 118, 1340
Vrba, F. J. 1977, AJ, 82, 198
Ward-Thompson, D., Di Francesco, J., Hatchell, J., et al. 2007, PASP, 119, 855
Ward-Thompson, D., Kirk, J. M., Crutcher, R. M., et al. 2000, ApJL, 537, L135
Ward-Thompson, D., Pattle, K., Bastien, P., et al. 2017, ApJ, 842, 66
Ward-Thompson, D., Sen, A. K., Kirk, J. M., & Nutter, D. 2009, MNRAS, 398, 394
Wilking, B. A., Gagné, M., & Allen, L. E. 2008, in Handbook of Star-forming Regions, Volume II: The Southern Sky, Vol. 5, ed. B. Reipurth (San Francisco, CA: ASP Monograph Publications), 351